

# NUCLEAR AND HIGH-ENERGY ASTROPHYSICS

FRIDOLIN WEBER

*Joint Center for Nuclear Astrophysics, Department of Physics, University of Notre Dame, 225 Nieuwland Science Hall, Notre Dame, IN 46556-5670, USA*

*E-mail: fweber@nd.edu*

There has never been a more exciting time in the overlapping areas of nuclear physics, particle physics and relativistic astrophysics than today. Orbiting observatories such as the Hubble Space Telescope, Rossi X-ray Timing Explorer (RXTE), Chandra X-ray satellite, and the X-ray Multi Mirror Mission (XMM) have extended our vision tremendously, allowing us to see vistas with an unprecedented clarity and angular resolution that previously were only imagined, enabling astrophysicists for the first time ever to perform detailed studies of large samples of galactic and extragalactic objects. On the Earth, radio telescopes (e.g., Arecibo, Green Bank, Parkes, VLA) and instruments using adaptive optics and other revolutionary techniques have exceeded previous expectations of what can be accomplished from the ground. The gravitational wave detectors LIGO, LISA VIRGO, and Geo-600 are opening up a window for the detection of gravitational waves emitted from compact stellar objects such as neutron stars and black holes. Together with new experimental forefront facilities like ISAC, ORLaND and RIA, these detectors provide direct, quantitative physical insight into nucleosynthesis, supernova dynamics, accreting compact objects, cosmic-ray acceleration, and pair-production in high energy sources which reinforce the urgent need for a strong and continuous feedback from nuclear and particle theory and theoretical astrophysics. In my lectures, I shall concentrate on three selected topics, which range from the behavior of superdense stellar matter, to general relativistic stellar models, to strange quark stars and possible signals of quark matter in neutron stars.

## 1 Introduction

A forefront area of research, both experimental and theoretical, concerns the exploration of the subatomic structure of superdense matter and the determination of the equation of state – that is, the relation between pressure  $P$ , temperature  $T$  and density  $\epsilon$  – associated with such matter.<sup>1</sup> Knowing its properties is of key importance for our understanding of the physics of the early universe, its evolution in time to the present day, compact stars, various astrophysical phenomena, and laboratory physics. The high-temperature domain of the phase diagram of superdense matter is probed by relativistic heavy-ion colliders. Complementary to this, neutron stars contain cold superdense matter permanently in their centers (cf. Fig. 1), which make them superb astrophysical laboratories for probing the low-density high-density domain of the phase diagram of superdense matter.<sup>2,3</sup>

Neutron stars are dense, neutron-packed remnants of massive stars that blew apart in supernova explosions. They are typically about 10 kilometers across and spin rapidly, often making several hundred rotations per second. The discovery rate of new rotating neutron stars, spotted as pulsars by radio telescopes<sup>4,5</sup>, is rather high. To date about 1400 pulsars are known. Depending on star mass and rotational frequency, gravity compresses the matter in the core regions of pulsars up to more than ten times ( $\sim 1.5 \text{ GeV}/\text{fm}^3$ ) the density of ordinary atomic nuclei, thus providing a high-pressure environment in which numerous subatomic particle

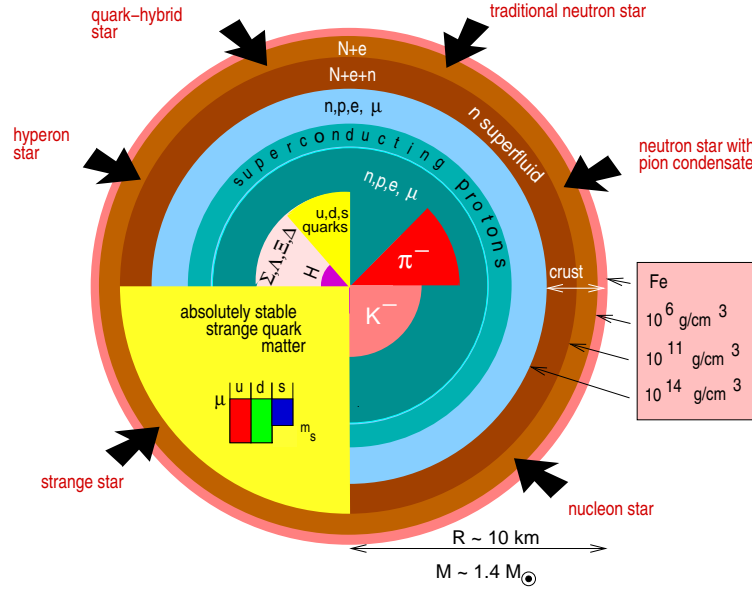


Figure 1. Competing structures and novel phases of subatomic matter predicted by theory to make their appearance in the cores ( $R \lesssim 8$  km) of neutron stars.<sup>3</sup>

processes plausibly compete with each other and novel phases of matter may exist. The most spectacular ones stretch from the generation of new baryonic particles (e.g.,  $\Sigma$ ,  $\Lambda$ ,  $\Xi$ ,  $\Delta$ ) to quark ( $u$ ,  $d$ ,  $s$ ) deconfinement to the formation of Boson condensates ( $\pi^-$ ,  $K^-$ , H-matter), as illustrated in Fig. 1. There are theoretical suggestions of even more exotic processes inside pulsars, such as the formation of absolutely stable quark matter, a configuration of matter even more stable than the most stable atomic nucleus,  $^{56}\text{Fe}$ ! In the latter event, pulsars would be largely composed of pure quark matter, eventually enveloped in thin nuclear crusts (bottom-left portion in Fig. 1). No matter which physical processes are actually realized inside neutron stars, each one leads to fingerprints, some more pronounced than others though, in the observable stellar quantities. Paired with the unprecedented wealth of new observational pulsar data, it seems to be within reach for the first time ever to seriously explore the subatomic structure of matter in the high-density low-temperature portion of its phase diagram from observed pulsar data. To this aim Einstein's field equation of relativistic gravity,

$$G^{\mu\nu} \equiv R^{\mu\nu} - \frac{1}{2}g^{\mu\nu}R = 8\pi T^{\mu\nu}(\epsilon, P(\epsilon)), \quad (1)$$

is to be solved in combination with the latest theories of the subatomic structure

of matter.<sup>3</sup> The latter follow according to the scheme

$$\frac{\partial \mathcal{L}(\{\phi\})}{\partial \phi} - \partial_\mu \frac{\partial \mathcal{L}(\{\phi\})}{\partial (\partial_\mu \phi)} = 0 \quad \Rightarrow \quad P(\epsilon), \quad (2)$$

where  $\mathcal{L}(\{\phi\})$  denotes a given stellar matter lagrangian.<sup>3</sup> In general,  $\mathcal{L}$  is a complicated functional of the numerous hadron and quark fields, collectively written as  $\{\phi\}$ , that acquire finite amplitudes up to the highest densities reached in the cores of neutron stars. According to what has been said just above, plausible candidates for  $\phi$  are the charged states of the SU(3) baryon octet,  $p, n, \Sigma, \Lambda, \Xi$ <sup>6</sup>, the charged states of the  $\Delta$ <sup>7,8</sup>,  $\pi^-$ <sup>9</sup> and  $K^-$ <sup>10,11,12,13,14</sup> mesons, as well as  $u, d, s$  quarks.<sup>15,16,17</sup> The conditions of chemical equilibrium and electric charge neutrality of stellar matter require the presence of leptons too, in which case  $\phi = e^-, \mu^-$ . Theories of superdense matter enter Einstein's field equation (1) via the energy-momentum tensor  $T^{\mu\nu}$ , which contains the equation of state of the stellar matter,  $P(\epsilon)$ . Because of the rather uncertain behavior of the matter at supernuclear densities, the models derived for the equation of state differ considerably with from each other. This has its origin in various sources such as: (1) the many-body technique used for the determination of the equation of state, (2) the model adopted for the nucleon-nucleon force, (3) assumptions about the fundamental building blocks of neutron star matter, (4) the inclusion of boson condensates, and (5) the considerations of a possible phase transition of confined hadronic matter into deconfined quark matter.<sup>3,18</sup>

In general Eqs. (1) and (2) were to be solved simultaneously since the particles move in curved spacetime whose geometry, determined by Einstein's field equations, is coupled to the total mass energy  $\epsilon$  of the matter. In the case of neutron stars, however, the long-range gravitational force can be cleanly separated from the short-range nuclear force so that Eqs. (1) and (2) decouple from each other. This simplifies the study of compact stellar objects considerably.

## 2 Models for the Equation of State of Superdense Neutron Star Matter

### 2.1 Nonrelativistic Models

For non-relativistic models, the starting point are phenomenological nucleon-nucleon interactions, denoted  $V_{ij}$ , which fit the nucleon-nucleon scattering data and the deuteron properties. In order to achieve the correct binding energy of nuclear matter at the empirical saturation density  $\rho_0$  ( $\rho_0 = 0.15$  nucleons/fm<sup>3</sup> which corresponds to a mass density of  $\epsilon = 2.5 \times 10^{14}$  g/cm<sup>3</sup>), two-nucleon potentials are supplemented with three-nucleon interactions  $V_{ijk}$ . The hamiltonian is then of the form

$$\mathcal{H} = \sum_i \left( \frac{-\hbar^2}{2m} \right) \nabla_i^2 + \sum_{i<j} V_{ij} + \sum_{i<j<k} V_{ijk}. \quad (3)$$

A proven many-body method frequently adopted to solve the associated many-body Schroedinger equation  $\mathcal{H}|\Psi \rangle = E|\Psi \rangle$  is the variational approach<sup>19,20</sup> where a

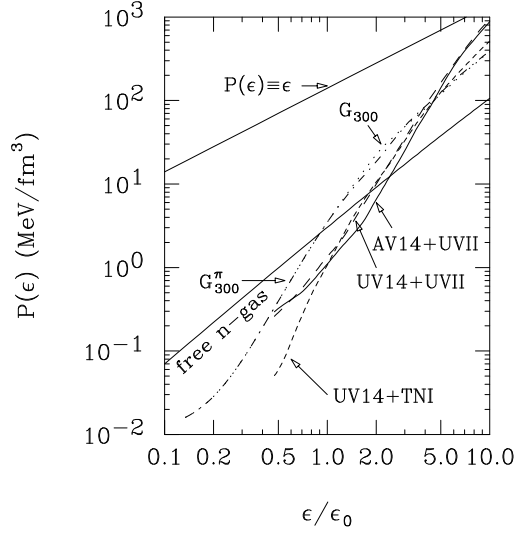


Figure 2. Graphical illustration of AV<sub>14</sub>+UVII, UV<sub>14</sub>+UVII, UV<sub>14</sub>+TNI, G<sub>300</sub>, and G<sub>300</sub><sup>π</sup>.<sup>3</sup>

variational trial function  $|\Psi_v\rangle$  is constructed from a symmetrized product of two-body correlation operators ( $F_{ij}$ ) acting on an unperturbed ground-state, i.e.,

$$|\Psi_v\rangle = \left[ \hat{S} \prod_{i<j} F_{ij} \right] |\Phi\rangle, \quad (4)$$

where  $|\Phi\rangle$  denotes the antisymmetrized Fermi-gas wave function,

$$|\Phi\rangle = \hat{A} \prod_j \exp(i\mathbf{p}_j \cdot \mathbf{x}_j). \quad (5)$$

The correlation operator contains variational parameters which are varied to minimize the energy per baryon for a given density  $\rho$ :<sup>19,20</sup>

$$E_v(\rho) = \min \left\{ \frac{\langle \Psi_v | \mathcal{H} | \Psi_v \rangle}{\langle \Psi_v | \Psi_v \rangle} \right\} \geq E_0. \quad (6)$$

As indicated,  $E_v$  constitutes an upper bound to the ground-state energy  $E_0$ . The energy density  $\epsilon(\rho)$  and pressure  $P(\rho)$  are obtained from Eq. (6) through the following manipulations:

$$\epsilon(\rho) = \rho (E_v(\rho) + m), \quad P(\rho) = \rho^2 \frac{\partial}{\partial \rho} E_v(\rho), \quad (7)$$

which can be combined to an equation of state of the form  $P(\epsilon)$  applicable to the stellar structure calculations.

A representative collection of non-relativistic nuclear equations of state is listed in Tables 1 and 2, where the following abbreviations are used: N = pure neutron matter; NP =  $n$ ,  $p$ , and leptons in chemical equilibrium; and  $K$  denotes the incompressibility (in MeV) of symmetric nuclear matter at saturation density. Several of

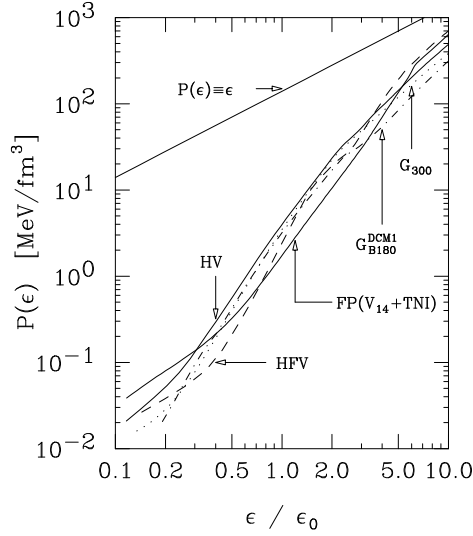


Figure 3. Graphical illustration of equations of state HV, HFV, FP(V<sub>14</sub>+TNI), G<sub>300</sub>, and G<sub>B180</sub><sup>DCM1</sup>.

Table 1. Non-relativistic models for the equation of state of neutron star matter.

EOS	Properties (see text)	References
WFF(UV <sub>14</sub> +TNI)	NP, $K=261$	22
WFF(UV <sub>14</sub> +UVII)	NP, $K=202$	22
WFF(AV <sub>14</sub> +UVII)	NP, $K=209$	22
FP(V <sub>14</sub> +TNI)	N, $K=240$	23
APR(A <sub>18</sub> +UIX)	NP	24
TF96	N, $K=234$	25,26,27,28

these equations of state are shown in Figs. 2 and 3 where the pressure is plotted as a function of total energy density (in units of the density of normal nuclear matter,  $\epsilon_0 = 140 \text{ MeV/fm}^3$ ). The Thomas-Fermi equation of state TF96 of Table 1 is based on the new Thomas-Fermi approach of Myers and Swiatecki.<sup>21</sup> The effective interaction  $v_{12}$  of this new approach consists of the Seyler-Blanchard potential<sup>29</sup>, generalized by the addition of one momentum dependent and one density dependent term,<sup>21</sup>

$$v_{12} = -\frac{2T_0}{\rho_0} Y(r_{12}) \times \left\{ \frac{1}{2}(1 \mp \xi) \alpha - \frac{1}{2}(1 \mp \zeta) \left( \beta \left( \frac{p_{12}}{k_{F_0}} \right)^2 - \gamma \frac{k_{F_0}}{p_{12}} + \sigma \left( \frac{2\bar{\rho}}{\rho_0} \right)^{\frac{2}{3}} \right) \right\}. \quad (8)$$

The upper (lower) sign in (8) corresponds to nucleons with equal (unequal) isospin. The quantities  $k_{F_0}$ ,  $T_0$  ( $= k_{F_0}^2/2m$ ), and  $\rho_0$  are the Fermi momentum, the Fermi energy and the particle density of symmetric nuclear matter. The potential's radial

Table 2. Nuclear matter properties of the equations of state compiled in Table 1.

EOS	$E/A$ (MeV)	$\rho_0$ (fm $^{-3}$ )	$K$ (MeV)	$M^*$ (MeV)	$a_{\text{sy}}$ (MeV)
WFF(UV $_{14}$ +TNI)	-16.6	0.157	261	0.65	30.8
WFF(UV $_{14}$ +UVII)	-11.5	0.175	202	0.79	29.3
WFF(AV $_{14}$ +UVII)	-12.4	0.194	209	0.66	27.6
FP(V $_{14}$ +TNI)	-16.00	0.159	240	0.64	-
APR(A $_{18}$ +UIX)	-16.00	0.16	-	-	-
TF96	-16.04	0.161	234	-	32.0

dependence is describe by the normalized Yukawa interaction

$$Y(r_{12}) = \frac{1}{4\pi a^3} \frac{e^{-r_{12}/a}}{r_{12}/a}. \quad (9)$$

Its strength depends both on the magnitude of the particles' relative momentum,  $p_{12}$ , and on an average of the densities at the locations of the particles. The parameters  $\xi$  and  $\zeta$  were introduced in order to achieve better agreement with asymmetric nuclear systems, and the behavior of the optical potential is improved by the term  $\sigma(2\bar{\rho}/\rho_0)^{2/3}$ . Here the average density is defined by  $\bar{\rho}^{2/3} = (\rho_1^{2/3} + \rho_2^{2/3})/2$ , where  $\rho_1$  and  $\rho_2$  are the relevant densities of the interacting particle (neutron or protons) at points 1 and 2. The potential's seven free parameters  $\alpha$ ,  $\beta$ ,  $\gamma$ ,  $\sigma$ ,  $\xi$ ,  $\zeta$ ,  $a$  are adjusted to the properties of finite nuclei, the parameters of the mass formula, and the behavior of the optical potential.<sup>27</sup> The nuclear matter properties at saturation obtained for TF96 are summarized in Table 2, where the listed quantities are: binding energy of normal nuclear matter at saturation density,  $E/A$ ; compression modulus,  $K$ ; effective nucleon mass,  $M^*$  ( $\equiv m^*/m$  where  $m$  denotes the free nucleon mass); and the asymmetry energy,  $a_{\text{sy}}$ . The new Thomas-Fermi force has the advantage over the standard Seyler-Blanchard interaction to not only reproduce the ground-state properties of finite nuclei and infinite symmetric nuclear matter, but also the optical potential and, as revealed by stellar structure calculations<sup>27</sup>, the properties of neutron stars as well. These features render the new Thomas-Fermi model very attractive for investigations of the properties of dense nuclear matter.

## 2.2 Relativistic Fieldtheoretical Models

Relativistic, field-theoretical theories of dense nuclear matter and finite nuclei have enjoyed a renaissance in recent years, and they have the virtue of describing nuclear matter at saturation, many features of finite nuclei, both spherical and deformed, and they extrapolate causally to high density.<sup>30</sup> The starting point of relativistic theories of superdense neutron star matter is a lagrangian of the following type,<sup>3</sup>

$$\mathcal{L}(x) = \sum_{B=p,n,\Sigma^{\pm,0},\Lambda,\Xi^{0,-},\Delta^{++,+0,-}} \mathcal{L}_B^0(x) \quad (10)$$

Table 3. Masses, quantum numbers (spin  $J_B$ , isospin  $I_B$ , strangeness  $S_B$ , hypercharge  $Y_B$ , third component of isospin  $I_{3B}$ ), and electric charges ( $q_B$ ) of baryons.

Baryon ( $B$ )	$m_B$ (MeV)	$J_B$	$I_B$	$S_B$	$Y_B$	$I_{3B}$	$q_B$
$n$	939.6	1/2	1/2	0	1	-1/2	0
$p$	938.3	1/2	1/2	0	1	1/2	1
$\Sigma^+$	1189	1/2	1	-1	0	1	1
$\Sigma^0$	1193	1/2	1	-1	0	0	0
$\Sigma^-$	1197	1/2	1	-1	0	-1	-1
$\Lambda$	1116	1/2	0	-1	0	0	0
$\Xi^0$	1315	1/2	1/2	-2	-1	1/2	0
$\Xi^-$	1321	1/2	1/2	-2	-1	-1/2	-1
$\Delta^{++}$	1232	3/2	3/2	0	1	3/2	2
$\Delta^+$	1232	3/2	3/2	0	1	1/2	1
$\Delta^0$	1232	3/2	3/2	0	1	-1/2	0
$\Delta^-$	1232	3/2	3/2	0	1	-3/2	-1

$$+ \sum_{M=\sigma,\omega,\pi,\rho,\eta,\delta,\phi} \left\{ \mathcal{L}_M^0(x) + \sum_{B=p,n,\dots,\Delta^{++},+^0,-} \mathcal{L}_{B,M}^{\text{Int}}(x) \right\} + \sum_{L=e^-, \mu^-} \mathcal{L}_L(x).$$

The subscript  $B$  runs over all baryon species that may become populated in dense neutron star matter (Table 3). The nuclear forces are mediated by a collection of scalar, vector, and isovector mesons<sup>31</sup> which is compiled in Table 4. The equations of motion that follow from Eq. (10) for the baryon fields are given by<sup>3</sup>

$$\begin{aligned} (i\gamma^\mu \partial_\mu - m_B) \psi_B(x) &= g_{\sigma B} \sigma(x) \psi_B(x) \\ &+ \left\{ g_{\omega B} \gamma^\mu \omega_\mu(x) + \frac{f_{\omega B}}{4m_B} \sigma^{\mu\nu} F_{\mu\nu}(x) \right\} \psi_B(x) \\ &+ \left\{ g_{\rho B} \gamma^\mu \boldsymbol{\tau} \cdot \boldsymbol{\rho}_\mu(x) + \frac{f_{\rho B}}{4m_B} \sigma^{\mu\nu} \boldsymbol{\tau} \cdot \mathbf{G}_{\mu\nu}(x) \right\} \psi_B(x) \\ &+ \frac{f_{\pi B}}{m_\pi} \gamma^\mu \gamma^5 (\partial_\mu \boldsymbol{\tau} \cdot \boldsymbol{\pi}(x)) \psi_B(x), \end{aligned} \quad (11)$$

where the standard field-theoretical notation of Ref. 32 is used. The meson fields in (11) obey the following field equations,<sup>3</sup>

$$\begin{aligned} (\partial^\mu \partial_\mu + m_\sigma^2) \sigma(x) &= - \sum_B g_{\sigma B} \bar{\psi}_B(x) \psi_B(x) - m_N b_N g_{\sigma N} (g_{\sigma N} \sigma(x))^2 \\ &- c_N g_{\sigma N} (g_{\sigma N} \sigma(x))^3, \end{aligned} \quad (12)$$

$$\begin{aligned} \partial^\mu F_{\mu\nu}(x) + m_\omega^2 \omega_\nu(x) &= \sum_B \left\{ g_{\omega B} \bar{\psi}_B(x) \gamma_\nu \psi_B(x) \right. \\ &\left. - \frac{f_{\omega B}}{2m_B} \partial^\mu (\bar{\psi}_B(x) \sigma_{\mu\nu} \psi_B(x)) \right\}, \end{aligned} \quad (13)$$

$$(\partial^\mu \partial_\mu + m_\pi^2) \boldsymbol{\pi}(x) = \sum_B \frac{f_{\pi B}}{m_\pi} \partial^\mu (\bar{\psi}_B(x) \gamma_5 \gamma_\mu \boldsymbol{\tau} \psi_B(x)), \quad (14)$$

Table 4. Mesons and their quantum numbers.<sup>33</sup> The entries are: spin  $J_M$ , parity  $\pi$ , isospin  $I_M$ , and mass  $m_M$  of meson  $M$ .

Meson ( $M$ )	$J_M^\pi$	$I_M$	Coupling	Mass (MeV)
$\sigma$	$0^+$	0	scalar	550
$\omega$	$1^-$	0	vector	783
$\pi^\pm$	$0^-$	1	pseudovector	140
$\pi^0$	$0^-$	1	pseudovector	135
$\rho$	$1^-$	1	vector	769
$\eta$	$0^-$	0	pseudovector	549
$\delta$	$0^+$	1	scalar	983
$\phi$	$1^-$	0	vector	1020
$K^+$	$0^-$	1/2	pseudovector	494
$K^-$	$0^-$	1/2	pseudovector	494

$$\partial^\mu \mathbf{G}_{\mu\nu}(x) + m_\rho^2 \rho_\nu(x) = \sum_B \left\{ g_{\rho B} \bar{\psi}_B(x) \boldsymbol{\tau} \gamma_\nu \psi_B(x) - \frac{f_{\rho B}}{2m_B} \partial^\lambda (\bar{\psi}_B(x) \boldsymbol{\tau} \sigma_{\mu\nu} \psi_B(x)) \right\}, \quad (15)$$

with the field tensors  $F^{\mu\nu}$  and  $\mathbf{G}^{\mu\nu}$  defined as  $F^{\mu\nu} = \partial^\mu \omega^\nu - \partial^\nu \omega^\mu$  and  $\mathbf{G}^{\mu\nu} = \partial^\mu \boldsymbol{\rho}^\nu - \partial^\nu \boldsymbol{\rho}^\mu$ . Equations (11) through (15) are to be solved simultaneously in combination with the neutron star matter constraints of electric charge neutrality and chemical equilibrium. The former can be written as

$$\sum_B q_B (2J_B + 1) \frac{p_{F,B}^3}{6\pi^2} - \sum_{\lambda=e,\mu} \frac{p_{F,\lambda}^3}{3\pi^2} - \varrho_M \Theta(\mu^M - m_M) = 0, \quad (16)$$

while chemical ( $\beta$ ) equilibrium is expressed as

$$\mu^B = \mu^n - q_B \mu^e, \quad (17)$$

where  $\mu^n$  and  $\mu^e$  denote the chemical potentials of neutrons and electrons whose knowledge is sufficient to determine the chemical potential of any other baryon present in the system. The only mesons that may plausibly condense (density  $\rho_M$ ) in neutron star matter are the  $\pi^-$ <sup>9,34</sup> or the  $K^-$ <sup>10,35,36,37</sup>. Equations (16) and (17) leads to constraints on the Fermi momenta of baryons and leptons,  $k_{F_B}$  and  $k_{F_L}$  respectively. The leptons in neutron star matter can be treated as free particles, which obey the following Dirac equation,

$$(i\gamma^\mu \partial_\mu - m_L) \psi_L(x) = 0, \quad (18)$$

with  $L = e^-, \mu^-$ . An elegant mathematical framework that enables one to solve the equations of motion (11) through (18) is the relativistic Greens function method, which is outlined next. The starting point is the Martin-Schwinger hierarchy of coupled Greens functions.<sup>38</sup> In the lowest order, the Martin-Schwinger hierarchy can be truncated by factorizing the four-point Greens function  $g_2(1, 2; 1'2')$ , where primed (unprimed) arguments refer to ingoing (outgoing) fermions, into a product

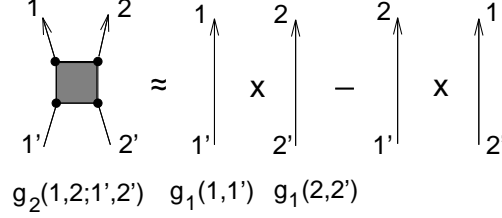


Figure 4. Factorization of four-point baryon Green function  $g_2$  into antisymmetrized products of two-point baryon Green functions,  $g_1 \times g_1$ . Direct (Hartree) and exchange (Fock) contribution are shown. This factorization scheme truncates the many-body equations at the Hartree-Fock level.

of two-point Greens functions  $g_1(1; 1')$ , as schematically shown in Fig. 4. This leads to the well-known relativistic Hartree (i.e., mean-field) and Hartree-Fock approximations. The  $T$ -matrix approximation, also known as ladder ( $\Lambda$ ) approximation, goes beyond Hartree and Hartree-Fock by truncating the Martin-Schwinger hierarchy by factorizing the six-point Greens function  $g_3(123; 1'2'3')$  into products of four-point and two-point functions by means of which dynamical two-particle correlations in matter, which are connected to a two-body boson-exchange potential  $v$ , are taken into account. The  $T$  matrix (effective two-particle interaction in matter) is computed from an integral equation of the following type, <sup>3</sup>

$$T = v - v^{\text{ex}} + \int v \Lambda T, \quad (19)$$

with  $\Lambda$  the baryon-baryon propagator in intermediate scattering states. In the framework of the so-called  $\Lambda^{00}$  approximation, the baryons in intermediate states propagate as free particles, leading to a  $\Lambda \approx \Lambda^{00} \equiv i g_1^0 g_1^0$ . This is in sharp contrast to the relativistic Brueckner-Hartree-Fock (RBHF) approximation where the intermediate baryons are coupled to the nuclear background and, therefore, are constrained to scattering states outside their respective Fermi seas.<sup>39,40,41</sup> The basic input quantity in Eq. (19) is the nucleon-nucleon interaction in free space. Representative models are, for instance, the Bonn meson-exchange model <sup>31</sup> and the boson-exchange potentials of Brockmann and Machleidt.<sup>42</sup> A characteristic feature of these potentials is that their parameters are adjusted to the relativistic two-nucleon scattering data and the properties of the deuteron. In this respect a parameter-free treatment of the many-body problem is achieved. The Born approximation to the  $T$ -matrix, which merely sums numerous boson-exchange potentials,

$$\langle 12 | v | 1'2' \rangle = \sum_{M=\sigma,\omega,\pi,\rho,\eta,\delta,\phi} \delta_{11'}^4 \Gamma_{11'}^M \Delta_{12}^M \Gamma_{22'}^M \delta_{22'}^4, \quad (20)$$

neglects dynamical correlations among baryons. It is this approximation which reduces the ladder approximation to the relativistic Hartree and Hartree-Fock approximations.<sup>3</sup> The symbols  $\Gamma^M$  in Eq. (20) stands for the various meson-nucleon vertices, and  $\Delta^M$  denotes the free meson propagator of a meson of type  $M$  whose explicit forms are given Ref. <sup>3</sup>. The baryon self-energy, or mass operator, is obtained

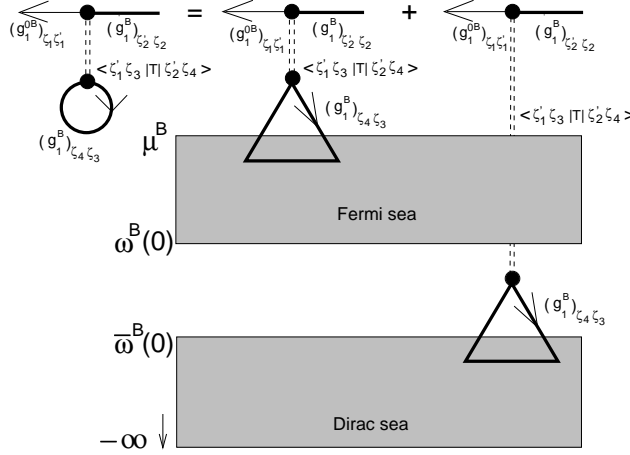


Figure 5. Graphical representation of  $g_1^{0B} \Sigma^B g_1^B$  of Dyson's equation (22). The Fermi sea of each baryon is filled up to the highest single-particle energy state,  $\mu^B$ . The infinite Dirac sea is filled with antibaryons, which too modify the motion of the baryons. The Fermi and Dirac-sea graphs are referred to as medium and vacuum polarization contributions, respectively.<sup>30,43</sup>

from the  $T$  matrix according to<sup>3</sup>

$$\Sigma^B = i \sum_{B'=p,n,\Sigma^{\pm,0},\Lambda,\Xi^{0,-},\Delta^{++,+},0,-} \int \left[ \text{tr} \left( T^{BB'} g_1^{B'} \right) - T^{BB'} g_1^{B'} \right], \quad (21)$$

where  $B'$  sums all the charged baryon states whose thresholds are reached in neutron star matter treated within this framework. The baryon Greens functions  $g_1^B$  in Eq. (21) are given as solutions of Dyson's equation,

$$g_1^B = g_1^{0B} + g_1^{0B} \Sigma^B (\{g_1^{B'}\}) g_1^B, \quad (22)$$

which terminates the set of equations to be solved self-consistently. The diagrammatic representation of the second term of Dyson's equation is shown in Fig. 5. It is this term which corrects the free Greens function for medium effects originating from the presence of Fermi seas of filled baryons. The equation of state follows from the stress-energy density tensor,  $T_{\mu\nu}$ , of the system as<sup>3</sup>

$$E(\rho) = \langle T_{00} \rangle / \rho - m, \quad \text{where} \quad (23)$$

$$T_{\mu\nu}(x) = \sum_{\chi=B,L} \partial_\nu \psi_\chi(x) \frac{\partial \mathcal{L}(x)}{\partial (\partial^\mu \psi_\chi(x))} - g_{\mu\nu} \mathcal{L}(x). \quad (24)$$

The pressure is obtained from  $E(\rho)$  as in Eq. (7).

A broad collection of relativistic models for the equation of state of superdense neutron star matter is compiled in Table 5. The specific properties of these equations of state are described in Table 6, where the following abbreviations are used: N = pure neutron; NP =  $n, p$ , leptons;  $\pi$  = pion condensation; H = composed of  $n, p$ , hyperons ( $\Sigma^{\pm,0}, \Lambda, \Xi^{0,-}$ ), and leptons;  $\Delta$  =  $\Delta_{1232}$ -resonance;  $K^-$  = condensate of negatively charged kaons; and  $K$  = incompressibility (in MeV). All equations of

Table 5. Relativistic, field-theoretical models for the equation of state of neutron star matter.

EOS	Properties (see text)	References
$G_{225}^{\text{DCM1}}$	H, $K=225$	44
$G_{265}^{\text{DCM2}}$	H, $K=265$	44
$G_{M78}^{K240}$	H, $K=240$	45
$G_{300}$	H, $K=300$	46
$G_{300}^{K^-}$	H, $K^-, K=300$	46
$G_{200}^{\pi}$	H, $\pi, K=200$	47
$G_{300}^{\pi}$	H, $\pi, K=300$	46
HV	H, $K=285$	6,7
$\Lambda_{\text{Bonn}}^{00} + \text{HV}$	H, $K=186$	48
HFV	H, $\Delta, K=376$	7
$\Lambda_{\text{HEA}}^{00} + \text{HFV}$	H, $\Delta, K=115$	48
$\Lambda_{\text{BroB}}^{\text{BHF}} + \text{HFV}$	H, $\Delta, K=249$	39,40,41

Table 6. Nuclear matter properties of the equations of state compiled in Table 5.

EOS	$E/A$ (MeV)	$\rho_0$ ( $\text{fm}^{-3}$ )	$K$ (MeV)	$M^*$ (MeV)	$a_{\text{sy}}$ (MeV)
$G_{225}^{\text{DCM1}}$	-16.0	0.16	225	0.796	32.5
$G_{265}^{\text{DCM2}}$	-16.0	0.16	265	0.796	32.5
$G_{M78}^{K240}$	-16.3	0.153	240	0.78	32.5
$G_{300}$	-16.3	0.153	300	0.78	32.5
$G_{300}^{K^-}$	-16.3	0.153	300	0.78	32.5
$G_{200}^{\pi}$	-15.95	0.145	200	0.8	36.8
$G_{300}^{\pi}$	-16.3	0.153	300	0.78	32.5
HV	-15.98	0.145	285	0.77	36.8
$\Lambda_{\text{Bonn}}^{00} + \text{HV}$	-11.9	0.134	186	0.79	34
HFV	-15.54	0.159	376	0.62	30
$\Lambda_{\text{HEA}}^{00} + \text{HFV}$	-8.7	0.132	115	0.82	29
$\Lambda_{\text{BroB}}^{\text{BHF}} + \text{HFV}$	-15.73	0.172	249	0.73	34.3

state of this collection account for neutron star matter in full baryonic equilibrium. A few selected equations of state of this collection are shown in Fig. 3. An inherent feature of relativistic equations of state is that they do not violate causality, i.e., the velocity of sound given by  $v_s = \sqrt{dP/d\epsilon}$  is smaller than the velocity of light at all densities. This is not the case for most non-relativistic models for the equation of state. Among the latter, WFF(UV<sub>14</sub> + TNI), APR(A<sub>18</sub> + UIX), and the TF96 models for the equation of state do not violate causality up to densities relevant for the construction of models of neutron stars from them.

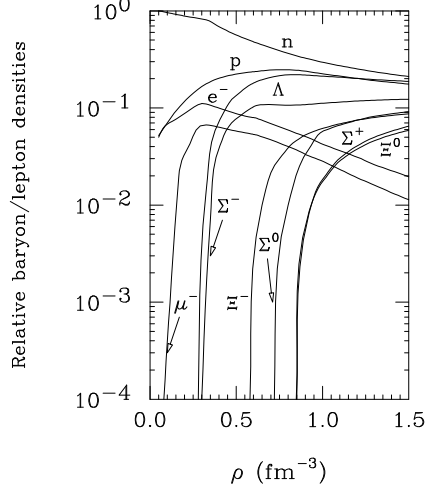


Figure 6. Baryon-lepton composition, normalized to the total baryon density  $\rho$ , of neutron star matter computed for HV.

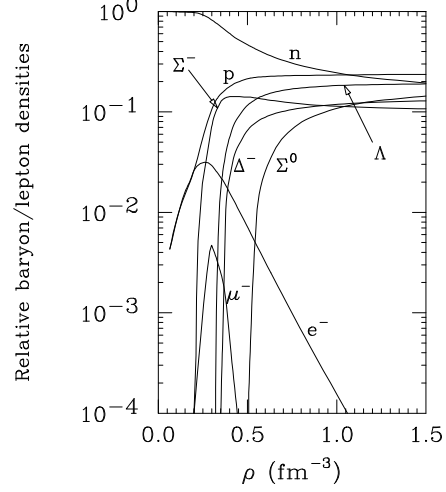


Figure 7. Same as figure 6, but computed for HFV.

### 2.3 Baryon-Lepton Composition of Neutron Star Matter

At densities lower than the density of normal nuclear matter,  $\epsilon_0$  ( $= 140 \text{ MeV}/\text{fm}^3$ ), neutron star matter consists of only  $p, n, e^-$ , and  $\mu^-$  whose densities are determined by the matter equations (16) through (22). At densities larger than  $\epsilon_0$  the more massive baryon states  $\Sigma^{\pm,0}, \Lambda, \Xi^{0,-}, \Delta^{++,\pm,0}$  become populated since their chemical potentials,  $\mu^B$ , become larger than the lowest-lying energy eigenstates  $\omega^B(\mathbf{p} = 0)$  of these particles,

$$\mu^B \equiv \mu^n - q_B \mu^e \geq \omega^B(\mathbf{p} = 0). \quad (25)$$

In relativistic field theory, the energy eigenstates are given by<sup>3</sup>

$$\omega^B(\mathbf{p}) = \Sigma_0^B(\omega^B(\mathbf{p}), \mathbf{p}) + I_{3B} \Sigma_{03}^B(\omega^B(\mathbf{p}), \mathbf{p}) + [m_B + \Sigma_S^B(\omega^B(\mathbf{p}), \mathbf{p})], \quad (26)$$

while in the non-relativistic case one has

$$\omega^B(\mathbf{p}) = \frac{1}{2m_B} \mathbf{p}^2 + \Sigma^B(\mathbf{p}), \quad (27)$$

where  $\Sigma^B$  denotes the non-relativistic one-particle potential felt by a baryon in matter. Since the chemical potentials  $\mu^n$  and  $\mu^e$  are positive and the self-energies  $\Sigma_{03}^B$  are negative ( $\Sigma_{03}^B$  is proportional to the difference of proton and neutron densities, which is negative for neutron star matter because of its neutron excess), it follows from Eq. (25) that (i) negatively charged baryons are charge-favored, and (ii) baryons having the opposite isospin orientation as the neutron (i.e.,  $I_{3B} > 0$ ) are isospin-favored.<sup>6</sup> The physical reason behind item (i) is that negatively charged baryons replace electrons with high Fermi momenta, while (ii) is making the matter more isospin symmetric. Both items enable neutron star matter to settle down in an

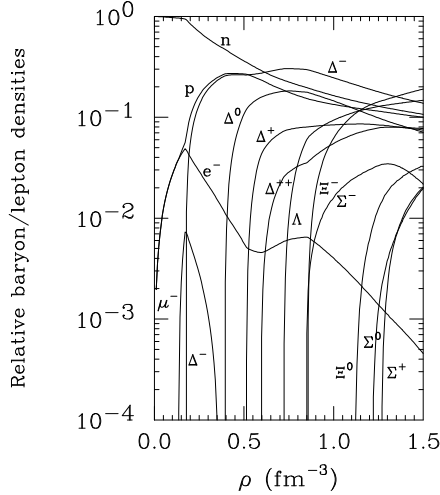


Figure 8. Same as figure 6, but for RBHF1 parameter set (see Ref. <sup>3</sup>). The hyperons are non-universally coupled, the  $\Delta$ 's universally.

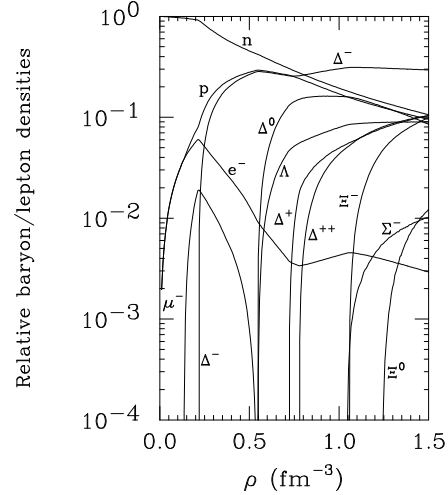


Figure 9. Same as Fig. 8, but for non-universally coupled hyperons and  $\Delta$ 's.<sup>8</sup>

energetically more favorable state. Figures 6 through 9 illustrate possible particle compositions of neutron star matter computed for different many-body techniques as well as different nuclear forces. One sees that in relativistic Hartree (HV) the  $\Lambda$  hyperon, which remains unaffected by the effects (i) and (ii) since its electric charge  $q_\Lambda = 0$  and the third component of isospin  $I_{3\Lambda} = 0$ , has the lowest threshold of all hyperons. In the case of relativistic Hartree-Fock (HFV), the charge favored but isospin unfavored  $\Sigma^-$  possesses the lowest threshold, and the  $\Delta$  makes its appearance too. The latter is also the case for relativistic Brueckner-Hartree-Fock type calculations.<sup>8</sup> The important net effect of all these new degrees of freedom is a softening of the equation of state at supernuclear densities, which reduces the maximum mass of a neutron star.

#### 2.4 H-dibaryons

A novel particle that may make its appearance in the center of a neutron star is the H-dibaryon, a doubly strange six-quark composite with spin and isospin zero, and baryon number two.<sup>49</sup> Since its first prediction in 1977, the H-dibaryon has been the subject of many theoretical and experimental studies as a possible candidate for a strongly bound exotic state. In neutron stars, which may contain a significant fraction of  $\Lambda$  hyperons (Figs. 6 through 9), the  $\Lambda$ 's could combine to form H-dibaryons, which could give way to the formation of H-matter at densities somewhere between  $3\epsilon_0$  and  $6\epsilon_0$  depending on the in-medium properties of the H-dibaryon.<sup>50,51,52</sup> This could cause a significant softening of the equation of state as shown in Fig. 10 (curves labeled  $U_H$ ). In Ref. <sup>50</sup> it was shown that H-dibaryons with a vacuum mass of about 2.2 GeV and a moderately attractive potential in

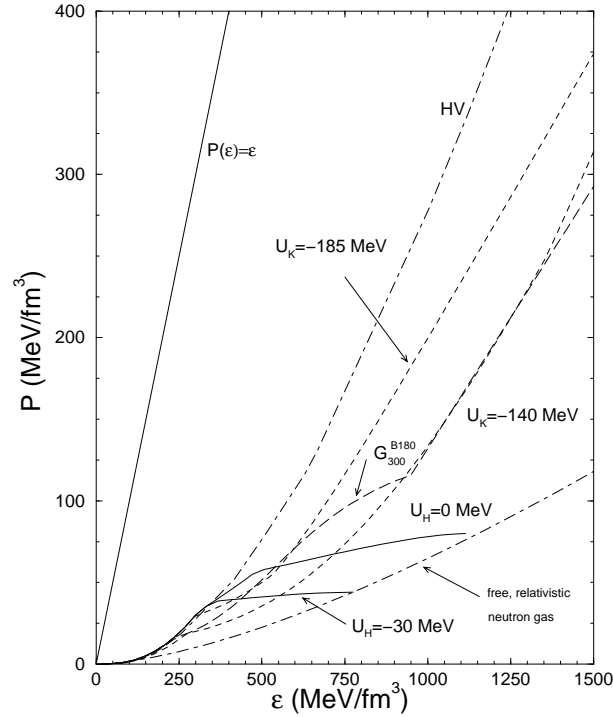


Figure 10. Models for the equation of state of neutron star matter.<sup>3</sup>

the medium of about  $U_H = -30$  MeV could go into a Bose condensate in the cores of neutron stars if the limiting star mass is about that of the Hulse-Taylor pulsar PSR 1913+16,  $M = 1.444 M_\odot$ . Conversely, if the medium potential were moderately repulsive, around  $U_H = +30$  MeV, the formation of H-dibaryons may only take place in heavier neutron stars of mass  $M \gtrsim 1.6 M_\odot$ . If indeed formed, however, H-matter may not remain dormant in neutron stars but, because of its instability against compression could trigger the conversion of neutron stars into hypothetical strange stars.<sup>52,53,54</sup>

### 2.5 Condensation of $K^-$ Mesons

Once the reaction

$$e^- \rightarrow K^- + \nu \quad (28)$$

becomes possible in a neutron star, it becomes energetically advantageous for the star to replace the fermionic electrons with the bosonic  $K^-$  mesons. Whether or not this actually happens depends on how quickly the  $K^-$  drops with density in dense matter (Fig. 11). An analysis of the KaoS data<sup>60</sup> shows that the attraction from nuclear matter may bring the  $K^-$  mass down to  $m_{K^-}^* \simeq 200$  MeV at  $\rho \sim 3\rho_0$ .

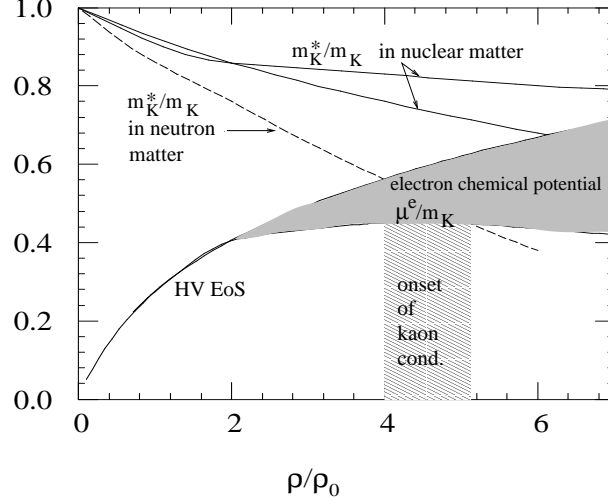


Figure 11. Effective kaon mass in nuclear and neutron star matter.<sup>55,56,57,58,59</sup>

For neutron-rich matter, the  $K^-$  mass may drop as<sup>11,12,13,14</sup>

$$m_{K^-}^*(\rho) \simeq m_{K^-} \left( 1 - 0.2 \frac{\rho}{\rho_0} \right), \quad (29)$$

with  $m_K = 495$  MeV the  $K^-$  vacuum mass. Combining this relation with the outcome for  $\mu^e$  shown in Fig. 11 shows that the threshold condition for the onset of  $K^-$  condensation,  $\mu^e = m_{K^-}^*$  would be fulfilled at densities  $\rho \gtrsim 3\rho_0$ , which are easily reached in neutron stars.

### 2.6 Quark Deconfinement

The phase transition between confined hadronic matter and quark matter is characterized by the conservation of baryon charge and electric charge. The Gibbs condition for phase equilibrium then is that the two associated chemical potentials  $\mu^n$  and  $\mu^e$ , corresponding to baryon and electric charge conservation, and the pressure in the two phases be equal,

$$P_H(\mu^n, \mu^e, \{\phi\}, T) = P_Q(\mu^n, \mu^e, T). \quad (30)$$

Here  $P_H$  denoted the pressure of hadronic matter computed for a hadronic Lagrangian  $\mathcal{L}(\{\phi\})$  as given in Eq. (10). The pressure of quark matter,  $P_Q$ , is obtainable from the bag model.<sup>17</sup> The quark chemical potentials  $\mu^u, \mu^d, \mu^s$  are related to the baryon and charge chemical potentials as

$$\mu^u = \frac{1}{3} \mu^n - \frac{2}{3} \mu^e, \quad \mu^d = \mu^s = \frac{1}{3} \mu^n + \frac{1}{3} \mu^e. \quad (31)$$

Equation (30) is to be supplemented with the two global relations for conservation of baryon charge and electric charge within an unknown volume  $V$  containing  $A$

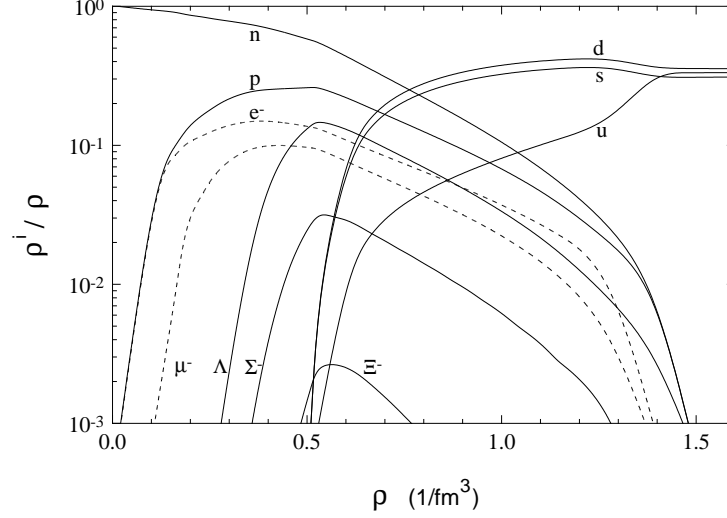


Figure 12. Sample composition of chemically equilibrated neutron (quark-hybrid) star matter.<sup>3,62</sup>

baryons.<sup>61</sup> The first one is given by

$$\rho \equiv \frac{A}{V} = (1 - \chi) \rho_H(\mu^n, \mu^e, T) + \chi \rho_Q(\mu^n, \mu^e, T), \quad (32)$$

where  $\chi \equiv V_Q/V$  denotes the volume proportion of quark matter,  $V_Q$ , in the unknown volume  $V$ , and  $\rho_i$  ( $i = H, Q, L$ ) is the particle number density. Global neutrality of electric charge within the volume  $V$  can be written as

$$0 = \frac{Q}{V} = (1 - \chi) q_H(\mu^n, \mu^e, T) + \chi q_Q(\mu^n, \mu^e, T) + q_L, \quad (33)$$

with  $q_i$  the electric charge densities of hadrons, quarks, and leptons. For a given temperature  $T$ , Eqs. (30) through (33) serve to determine the two independent chemical potentials and the volume  $V$  for a specified volume fraction  $\chi$  of the quark phase in equilibrium with the hadronic phase. After completion  $V_Q$  is obtained as  $V_Q = \chi V$ . Through Eqs. (30) to (33), the chemical potentials obviously depend on the proportion  $\chi$  of the phases in equilibrium, and hence so also all properties that depend on them, the energy densities, baryon and charge densities of each phase,

Table 7. Models for the equation of state of neutron star matter accounting for quark deconfinement.

EOS	Properties (see text)	Reference
$G_{B180}^{DCM1}$	H,Q, $K=225$ , $B^{1/4} = 180$	61,63
$G_{B180}^{DCM2}$	H,Q, $K=265$ , $B^{1/4} = 180$	61,63
$G_{B180}^{K240}$	H,Q, $K=240$ , $B^{1/4} = 180$	45
$G_{B180}^{K300}$	H,Q, $K=300$ , $B^{1/4} = 180$	45

Table 8. Nuclear matter properties of the equations of state compiled in Table 7.

EOS	$E/A$ (MeV)	$\rho_0$ (fm $^{-3}$ )	$K$ (MeV)	$M^*$ (MeV)	$a_{\text{sy}}$ (MeV)
$G_{\text{B180}}^{\text{DCM1}}$	-16.0	0.16	225	0.796	32.5
$G_{\text{B180}}^{\text{DCM2}}$	-16.0	0.16	265	0.796	32.5
$G_{\text{B180}}^{\text{K240}}$	-16.3	0.153	240	0.78	32.5
$G_{\text{B180}}^{\text{K300}}$	-16.3	0.153	300	0.70	32.5

and the common pressure. For the mixed phase, the volume proportion of quark matter varies from  $0 \leq \chi \leq 1$ , and the energy density is the linear combination of the two phases,<sup>61</sup>

$$\epsilon = (1 - \chi) \epsilon_{\text{H}}(\mu^n, \mu^e, \{\phi\}, T) + \chi \epsilon_{\text{Q}}(\mu^n, \mu^e, T). \quad (34)$$

By solving the models of confined and deconfined phases in both pure phases and in the mixed phase, we can compute the baryon, lepton and quark populations in neutron star matter from Eqs. (30) through (33). One such sample outcome is shown in Fig. 12. Three features emerge immediately from this population. Firstly, one sees that the transition from pure hadronic matter to the mixed phase occurs at rather low density of about  $3 \rho_0$ . Depending on the bag constant and the underlying nuclear many-body approximation, threshold values even as small as about  $2 \rho_0$  can be obtained.<sup>61,62</sup> Secondly, the lepton density saturates as soon as deconfined quark matter is generated, since charge neutrality can be achieved more economically among the baryon-charge carrying particles themselves. Thirdly, the presence of quark matter enables the hadronic regions of the mixed phase to arrange themselves to be more isospin symmetric than in the pure phase by transferring charge to the quark phase in equilibrium with it. Symmetry energy will be lowered thereby at only a small cost in rearranging the quark Fermi surfaces. Thus the mixed phase region consists of positively charged nuclear matter and negatively charged quark matter. Models for the equation of state of neutron star matter which account for quark deconfinement are listed in Tables 7 and 8. A graphical illustration of these equations of state is shown in Fig. 13.

### 3 Observed Neutron Star Properties

Orbiting observatories such as the Hubble Space Telescope, the Chandra X-ray satellite, and the X-ray Multi Mirror Mission have extended our vision tremendously, allowing us to look at neutron stars with an unprecedented clarity and angular resolution that previously were only imagined. The properties of such objects such as masses, rotational frequencies, radii, moments of inertia, redshifts, and temperatures are known to be sensitive to the adopted microscopic model for the nucleon-nucleon interaction and thus to the nuclear equation of state.<sup>3,64</sup> Hence by means of comparing theoretically determined values for these quantities with observed ones one may be able to constrain the behavior of superdense matter from the (unprecedented wealth of new) observational pulsar data. In the following we briefly summarize several important star properties.



Observationally, the searches for rapidly rotating radio pulsars are biased, being least sensitive to short periods. Therefore the world's data of radio pulsars are unlikely to represent the true underlying population of fast pulsars.<sup>71</sup> Most of the large surveys have had very poor sensitivity to millisecond pulsars with rotational periods below about 4 ms, thus presumably distorting the statistics on pulsar periods. The present cutoff in short periods at about 1 ms is therefore possibly only an artifact of the search sensitivity.

### 3.3 Radii

Direct radius determinations for neutron stars do not exist. However, combinations of data of 10 well-observed X-ray bursters with special theoretical assumptions lead Van Paradijs<sup>72</sup> to the conclusion that the emitting surface has a radius of about 8.5 km. This value, however, may be underestimated by a factor of two.<sup>73</sup> Fujimoto and Taam derived from the observational data of the X-ray burst source MXB 1636–536, under somewhat uncertain theoretical assumptions, a neutron star mass and radius of  $1.45 M_{\odot}$  and 10.3 km.<sup>74</sup> An error analysis led them to predicting mass and radius ranges of 1.28 to  $1.65 M_{\odot}$  and 9.1 to 11.3 km, respectively. Very recently the nearby, isolated neutron star RXJ 185635–3754<sup>75,76</sup> has attracted particular attention because of its interpretation as a possible strange quark star.<sup>77</sup> (The physics of strange quark stars will be discussed in Sect. 5.) The observed X-ray flux and temperature from this object, if originating from a uniform blackbody, appears to correspond to an effective stellar radius significantly smaller than  $\sim 10$  km, the canonical neutron star radius. This follows from the relation

$$R_{\infty} = R \left( 1 - \frac{2M}{R} \right)^{-1/2} \approx 7 \frac{D}{120 \text{ pc}} \text{ km}, \quad (35)$$

where  $R$  is the neutron star radius,  $M$  its mass, and  $D$  the distance to the star. One major uncertainty in (35) is buried in the numerical coefficient, which could increase by 50% or more if the star's surface temperature is not uniform. Moreover, the existence of an atmosphere on this neutron star could alter the coefficient probably even more strongly.<sup>78</sup> The other major uncertainty in obtaining a radius is the star's distance which, however, has now been determined to be  $D = 117 \pm 12$  pc<sup>79</sup>, nearly double the originally published distance. Taking these considerations into account, the interpretation of RXJ 185635–3754 as a quark star appears questionable.<sup>79</sup>

### 3.4 Moment of Inertia

Another global neutron star property is the moment of inertia,  $I$ . Early estimates of the energy-loss rate from pulsars spanned a wide range of  $I$ , i.e.,  $7 \times 10^{43} < I < 7 \times 10^{44} \text{ g/cm}^3$ .<sup>80</sup> From the luminosity of the Crab nebula ( $\sim 2 - 4 \times 10^{38} \text{ erg/sec}$ ), several authors have found a lower bound on the moment of inertia of the pulsar given by  $I \gtrsim 4 - 8 \times 10^{44} \text{ g cm}^2$ .<sup>81,82,83</sup>

### 3.5 Redshift

Next we mention the neutron star redshift,  $z$ , which is given by

$$z = \left(1 - \frac{2M}{R}\right)^{-1/2} - 1, \quad (36)$$

with  $M$  and  $R$  the star's mass and radius. Liang has considered the neutron star redshift data base provided by measurements of  $\gamma$ -ray burst redshifted annihilation lines in the range 300 – 511 keV.<sup>84</sup> These bursts have widely been interpreted as gravitationally redshifted 511 keV  $e^\pm$  pair annihilation lines from the surfaces of neutron stars. From this he showed that there is tentative evidence to support a neutron star redshift range of  $0.2 \leq z \leq 0.5$ , with the highest concentration in the narrower range  $0.25 \leq z \leq 0.35$ . A particular role plays the source of the 1979 March 5  $\gamma$ -ray burst source, which has been identified with SNR N49 by its position. From the interpretation of its emission, which has a peak at  $\sim 430$  keV, as the 511 keV  $e^\pm$  annihilation line the resulting gravitational redshift has a value of  $z = 0.23 \pm 0.05$ .

### 3.6 Magnetic fields

Neutron stars are highly magnetized objects.<sup>85</sup> There is a general plausibility argument to the effect that, if internal magnetic flux in a star is conserved owing to high conductivity, then the surface magnetic field increases as  $R^{-2}$  where  $R$  is the stellar radius. Thus, if the sun were to collapse to neutron star dimensions (roughly a factor of  $7 \times 10^4$  in radius), one would magnify the general 1 G solar field to about  $5 \times 10^9$  G. This value, while being in good agreement with the magnetic field strength of  $B \sim 4 - 6 \times 10^{11}$  G estimated for the X-ray pulsar 1E 2259+586<sup>86</sup>, the central source in the supernova remnant G 109.1–1.0, is a bit shy of  $10^{12}$  G inferred from line features in the pulsed hard X-ray spectrum of Her X–1 and 4U 0115–63.<sup>87,88,89</sup> Which physical mechanisms might be important to create the extraordinarily strong magnetic fields of neutron stars is an open issue. One possible mechanism may be differential rotation of the stellar core, as proposed for planetary magnetic fields. Besides that, ferromagnetism has been examined as a possible magnetic field source, while differential rotation between say superfluid protons and normal electrons has been another suggestion.<sup>85</sup> Effects of strong magnetic fields on the structure of compact stars were studied, for instance, in Refs.<sup>90,91</sup> Particularly striking are so-called magnetars, which are interpreted as neutron stars with superstrong surface magnetic fields on the order of  $\sim 10^{15}$  G.<sup>92</sup> This translates to interior magnetic fields of up to  $\sim 10^{18}$  G, which is about the highest possible value a star can sustain.

### 3.7 Cooling Data

The detection of thermal photons from a stellar surface via X-ray observatories like ASCA and ROSAT serves as the principal window on the properties of a star. The surface temperatures of stars are derivable from the measured flux and spectrum. The cooling rate of a hot, young neutron star is primarily dependent at early times (first several thousand years) on the neutrino emissivity of the core's

Table 9. Overview of neutrino emitting processes relevant for neutron star cooling.<sup>3</sup>

Name	Particle processes	Efficiency
Modified Urca	$n + n \rightarrow n + p + e^- + \bar{\nu}_e$	slow
	$n + p + e^- \rightarrow n + n + \nu_e$	
Direct Urca	$n \rightarrow p + e^- + \bar{\nu}_e$	fast
	$p + e^- \rightarrow n + \nu_e$	
Quark modified Urca	$d + u + e^- \rightarrow d + d + \nu_e$	slow
	$u + u + e^- \rightarrow u + d + \nu_e$	
	$d + u + e^- \rightarrow d + s + \nu_e$	
	$u + u + e^- \rightarrow u + s + \nu_e$	
Quark direct Urca	$d \rightarrow u + e^- + \bar{\nu}_e$	fast
	$u + e^- \rightarrow d + \nu_e$	
	$s \rightarrow u + e^- + \bar{\nu}_e$	
	$u + e^- \rightarrow s + \nu_e$	
$\pi^-$ condensate	$n + \langle \pi^- \rangle \rightarrow n + e^- + \bar{\nu}_e$	fast
$K^-$ condensate	$n + \langle K^- \rangle \rightarrow n + e^- + \bar{\nu}_e$	fast
Quark bremsstrahlung	$Q_1 + Q_2 \rightarrow Q_1 + Q_2 + \nu + \bar{\nu}$	slow
Core bremsstrahlung	$n + n \rightarrow n + n + \nu_e + \bar{\nu}_e$	slow
	$n + p \rightarrow n + p + \nu_e + \bar{\nu}_e$	
	$e^- + p \rightarrow e^- + p + \nu_e + \bar{\nu}_e$	
Crust bremsstrahlung	$e^- + (A, Z) \rightarrow e^- + (A, Z) + \nu_e + \bar{\nu}_e$	slow

composition. The possible existence of Bose-Einstein condensates or quark matter enhance the neutrino emissivity from the core, leading to a more rapid early cooling (Table 9). Superfluidity, on the other hand, has the opposite effect on cooling. Quantitative constraints have been hampered by the relatively small number of young pulsars known, the complication that several of them also display non-thermal, beamed X-ray emission from their magnetospheres, and uncertainties in distance and interstellar absorption. Table 10 gives an overview of observed neutron star temperatures. Because of its unusually low temperature which appears to falls well below predictions from standard cooling models<sup>109</sup>, the neutron star in supernova remnant (SNR) 3C58 received much attention recently (see Sect. 6).

## 4 Properties of Neutron Star Models

### 4.1 Nonrotating Star Models

For many studies of neutron star properties it is sufficient to treat neutron star matter as a perfect fluid. The energy-momentum tensor of such a fluid is given by

$$T^{\mu\nu} = u^\mu u^\nu (\epsilon + P) + g^{\mu\nu} P, \quad (37)$$

where  $u^\mu$  and  $u^\nu$  are four-velocities defined as

$$u^\mu \equiv \frac{dx^\mu}{d\tau}, \quad u^\nu \equiv \frac{dx^\nu}{d\tau}. \quad (38)$$

Table 10. Ages  $\tau$  (in years) and luminosities  $L$  (in  $\text{erg s}^{-1}$ ) / temperatures  $T$  (in  $K$ ) of pulsars.<sup>3</sup>

Pulsar	SNR	$\log_{10} \tau$	$L$ or $T$	Refs.
1706-44		4.25	$\log_{10} L = 32.8 \pm 0.7$	93
1823-13		4.50	$\log_{10} L = 33.2 \pm 0.6$	94
2334+61		4.61	$\log_{10} L = 33.1 \pm 0.4$	95
0531+21	Crab	3.09	$\log_{10} L = 35.5 \pm 0.3$	96
1509-58	MSH 15-52	3.19	$\log_{10} L = 33.6 \pm 0.4$	97,98
0540-69		3.22	$\log_{10} L = 36.2 \pm 0.2$	99
1951+32	CTB 80	5.02	$\log_{10} L = 33.8 \pm 0.5$	100
1929+10		6.49	$\log_{10} L = 28.9 \pm 0.5$	101,102
0950+08		7.24	$\log_{10} L = 29.6 \pm 1.0$	103
J0437-47		8.88	$\log_{10} L = 30.6 \pm 0.4$	104
0833-45	Vela	4.05	$\log_{10} L = 32.9 \pm 0.2$	105
0656+14		5.04	$\log_{10} L = 32.6 \pm 0.3$	106
0630+18	Geminga	5.51	$\log_{10} L = 31.8 \pm 0.4$	107
1055-52		5.73	$\log_{10} L = 33.0 \pm 0.6$	108
J0205+6449	3C58	2.91	$\log_{10} T = 6.0334$	109

They are the components of the macroscopic velocity of the stellar matter with respect to the actual coordinate system that is being used to derive the stellar equilibrium equations. The production of curvature by the star's mass is specified by Einstein's field equations,

$$G_{\mu\nu} = 8\pi T_{\mu\nu}, \quad \text{where} \quad G_{\mu\nu} \equiv R_{\mu\nu} - \frac{1}{2} g_{\mu\nu} R \quad (39)$$

is the Einstein tensor. The Ricci tensor  $R_{\mu\nu}$  is obtained from the Riemann tensor  $R^\tau{}_{\mu\sigma\nu}$  by contraction, that is,  $R_{\mu\nu} = R^\tau{}_{\mu\sigma\nu} g^\sigma{}_\tau$  which leads to

$$R_{\mu\nu} = \frac{\partial}{\partial x^\nu} \Gamma_{\mu\sigma}^\sigma - \frac{\partial}{\partial x^\sigma} \Gamma_{\mu\nu}^\sigma + \Gamma_{\mu\sigma}^\kappa \Gamma_{\kappa\nu}^\sigma - \Gamma_{\mu\nu}^\kappa \Gamma_{\kappa\sigma}^\sigma, \quad (40)$$

with  $\Gamma_{\mu\nu}^\sigma$  the Christoffel defined as

$$\Gamma_{\mu\nu}^\sigma \equiv \frac{1}{2} g^{\sigma\lambda} \left( \frac{\partial}{\partial x^\nu} g_{\mu\lambda} + \frac{\partial}{\partial x^\mu} g_{\nu\lambda} - \frac{\partial}{\partial x^\lambda} g_{\mu\nu} \right). \quad (41)$$

The scalar curvature of spacetime  $R$  in Eq. (39), also known as Ricci scalar, follows from Eq. (40) as

$$R = R_{\mu\nu} g^{\mu\nu}. \quad (42)$$

Finally, we need to specify the metric of a non-rotating body in general relativity theory. Assuming spherical symmetry, the metric has the form

$$ds^2 = -e^{2\Phi(r)} dt^2 + e^{2\Lambda(r)} dr^2 + r^2 d\theta^2 + r^2 \sin^2\theta d\phi^2, \quad (43)$$

where  $\Phi(r)$  and  $\Lambda(r)$  are radially varying metric functions. Introducing the covariant components of the metric tensor,

$$g_{tt} = -e^{2\Phi}, \quad g_{rr} = e^{2\Lambda}, \quad g_{\theta\theta} = r^2, \quad g_{\phi\phi} = r^2 \sin^2\theta, \quad (44)$$

the non-vanishing Christoffel symbols of a spherically symmetric body are

$$\Gamma_{tt}^r = e^{2\Phi-2\Lambda} \Phi', \quad \Gamma_{tr}^t = \Phi', \quad \Gamma_{rr}^r = \Lambda', \quad \Gamma_{r\theta}^\theta = r^{-1}, \quad \Gamma_{r\phi}^\phi = r^{-1}, \quad \Gamma_{\theta\theta}^r = -r e^{-2\Lambda},$$

$$\Gamma_{\theta\phi}^\phi = \frac{\cos\theta}{\sin\theta}, \quad \Gamma_{\phi\phi}^r = -r \sin^2\theta e^{-2\Lambda}, \quad \Gamma_{\phi\phi}^\theta = -\sin\theta \cos\theta, \quad (45)$$

where accents denote differentiation with respect to the radial coordinate. From Eqs. (37), (39) and (45) one derives the structure equations of spherically symmetric neutron stars known as Tolman-Oppenheimer-Volkoff equations,<sup>110,111</sup>

$$\frac{dP}{dr} = -\frac{\epsilon(r)m(r)}{r^2} \frac{[1 + P(r)/\epsilon(r)] [1 + 4\pi r^3 P(r)/m(r)]}{1 - 2m(r)/r}. \quad (46)$$

Note that we use units for which the gravitational constant and velocity of light are  $G = c = 1$  so that  $M_\odot = 1.5$  km. The boundary condition to (46) is  $P(r = 0) \equiv P_c = P(\epsilon_c)$ , where  $\epsilon_c$  denotes the energy density at the star's center, which constitutes an input parameter. The pressure is to be computed out to that radial distance where  $P(r = R) = 0$  which determines the star's radius  $R$ . The mass contained in a sphere of radius  $r$  ( $\leq R$ ), denoted by  $m(r)$ , follows as

$$m(r) = 4\pi \int_0^r dr' r'^2 \epsilon(r'). \quad (47)$$

The star's total gravitational mass is thus given by  $M \equiv m(R)$ .

Figure 14 exhibits the gravitational masses of non-rotating neutron stars as a function of central energy density for a sample of equations of state of Tables 1 and 5. Each star sequence is shown up to densities that are slightly larger than those of the maximum-mass star (indicated by tick marks) of each sequence. Stars beyond the mass peak are unstable against radial oscillations and thus cannot exist stably (collapse to black holes) in nature. One sees that all equations of state are able to support non-rotating neutron star models of gravitational masses  $M \geq M(\text{PSR 1913+16})$ . On the other hand, rather massive stars of say  $M \gtrsim 2 M_\odot$  can only be obtained for those models of the equation of state that exhibit a rather stiff behavior at supernuclear densities. The largest maximum mass value,  $M = 2.2 M_\odot$ , is obtained for HFV, which is caused by the stiffening exchange term. Knowledge of the maximum mass value is of great importance for two reasons. Firstly, because the largest known neutron star mass imposes a lower bound on the maximum mass of a theoretical model. The current lower bound is about  $1.60 M_\odot$  [neutron star 4U 0900-40 ( $\equiv$  Vela X-1)] which does not set too stringent a constraint on the nuclear equation of state. The situation could easily change if an accurate future determination of the mass of this neutron star should result in a value that is close to its present upper bound of  $2.1 M_\odot$ . In this case most of the equations of state of our collection would be ruled out. The second reason is that the maximum mass is essential in order to identify black hole candidates.<sup>112,113</sup> For example, if the mass of a compact companion of an optical star is determined to exceed the maximum mass of a neutron star it must be a black hole. Since the maximum mass of stable neutron stars studied here is  $\sim 2.2 M_\odot$ , compact companions being more massive than that value are predicted to be black holes.

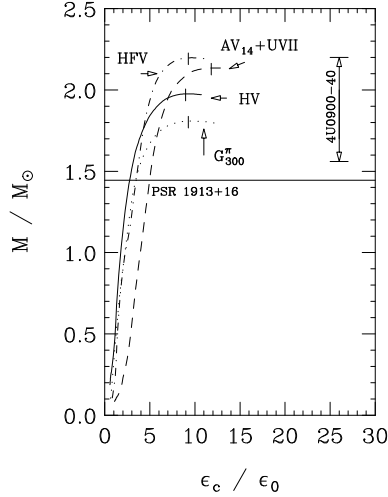


Figure 14. Non-rotating neutron star mass as a function of central density.<sup>3</sup>

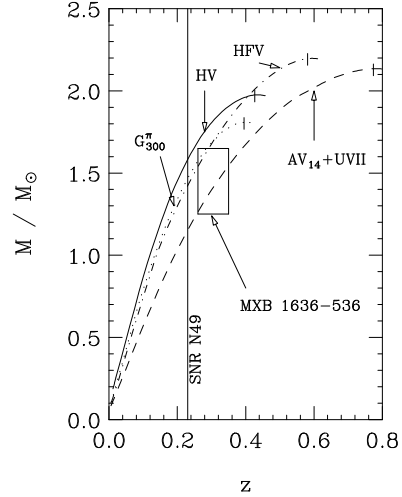


Figure 15. Non-rotating neutron star mass as a function of redshift.<sup>3</sup>

The neutron star mass as a function of gravitational redshift, defined in Eq. (36), is shown in Fig. 15. Maximum-mass stars have redshifts in the range  $0.4 \lesssim z \lesssim 0.8$ , depending on the stiffness of the equation of state. Neutron stars of typically  $M \approx 1.5 M_\odot$  (e.g., PSR 1913+16) are predicted to have redshifts in the considerably narrower range  $0.2 \leq z \leq 0.32$ . The rectangle covers masses and redshifts in the ranges of  $1.30 \leq M/M_\odot \leq 1.65$  and  $0.25 \leq z \leq 0.35$ , respectively. The former range has been determined from observational data on X-ray burst source MXB 1636–536<sup>74</sup>, while the latter is based on the neutron star redshift data base provided by measurements of gamma-ray burst pair annihilation lines.<sup>84</sup> From the redshift value of SNR N49 one would expect a neutron mass star of mass  $1.1 \lesssim M/M_\odot \lesssim 1.6$ . Figure 16 displays the radius as a function of gravitational redshift.

Figure 17 shows the moment of inertia of neutron stars, given by<sup>114</sup>

$$I(\Omega) = 4\pi \int_0^{\pi/2} d\theta \int_0^{R(\theta)} dr e^{\lambda+\mu+\nu+\psi} \frac{\epsilon + P(\epsilon)}{e^{2\nu-2\psi} - (\Omega - \omega)^2} \frac{\Omega - \omega}{\Omega}, \quad (48)$$

as a function of gravitational mass. In Newtonian mechanics one has for a sphere of uniform density  $I \propto R^2 M$ . The general relativistic expression for the moment of inertia, given in Eq. (48), is considerably more complicated as it accounts for the dragging effect of the local inertial frames (see Fig. 18) and the curvature of space-time.<sup>3</sup> Nevertheless the qualitative dependence of  $I$  on mass and radius as expressed in the classical expression remains valid. Estimates for the upper and lower bounds on the moment of inertia of the Crab pulsar derived from the pulsar's energy loss rate (labeled Rud72), and the lower bound on the moment of inertia derived from the luminosity of the Crab nebula (labeled Crab) are shown in Fig. 17. The arrows refer only to the value of the moment of inertial of the Crab pulsar

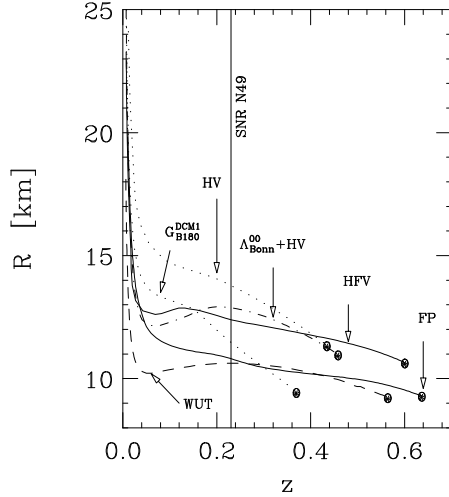


Figure 16. Radius as a function of redshift for a collection of equations of state.<sup>3</sup>

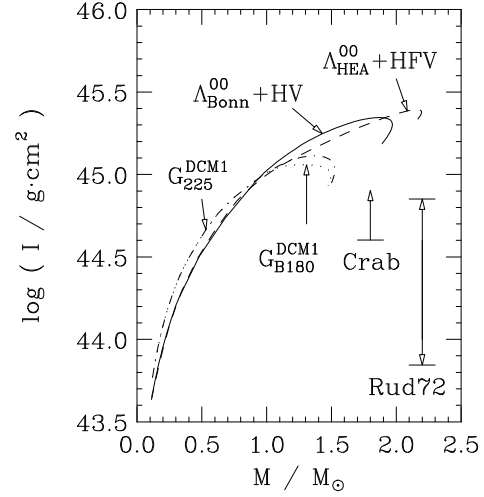


Figure 17. Moment of inertia as a function of mass for a collection of equations of state.<sup>3</sup>

and not to its mass, which is not known.

#### 4.2 Rotating Star Models

The stellar equations describing rotating compact stars are considerably more complicated than those of non-rotating compact stars.<sup>3</sup> These complications have their cause in the deformation of rotating stars plus the general relativistic effect of the dragging of local inertial frames. This reflects itself in a metric of the form<sup>3,115</sup>

$$ds^2 = -e^{2\nu} dt^2 + e^{2\psi} (d\phi - \omega dt)^2 + e^{2\mu} d\theta^2 + e^{2\lambda} dr^2, \quad (49)$$

where each metric function  $\nu$ ,  $\psi$ ,  $\mu$  and  $\lambda$  depends on the radial coordinate  $r$ , polar angle  $\theta$ , and implicitly on the star's angular velocity  $\Omega$ . The quantity  $\omega$  denotes the angular velocity of the local inertial frames, which are dragged along in the direction of the star's rotation. This frequency too depends on  $r$ ,  $\theta$  and  $\Omega$ . Of particular interest is the relative frame dragging frequency  $\bar{\omega}$  defined as  $\bar{\omega}(r, \theta, \Omega) \equiv \Omega - \omega(r, \theta, \Omega)$ , which typically increases from about 15% at the surface to about 60% at the center of a neutron star that rotates at its Kepler frequency.<sup>3</sup>

#### 4.3 Mass shedding versus Gravity Wave Emission

The Kepler frequency,  $\Omega_K$ , is the maximum frequency a star can have before mass loss (mass shedding) at the equator sets in. It sets an absolute upper limit on stable rapid rotation. In classical mechanics the expression for  $\Omega_K$ , determined by the equality between centrifuge and gravity, is readily obtained as  $\Omega_K = \sqrt{M/R^3}$ .

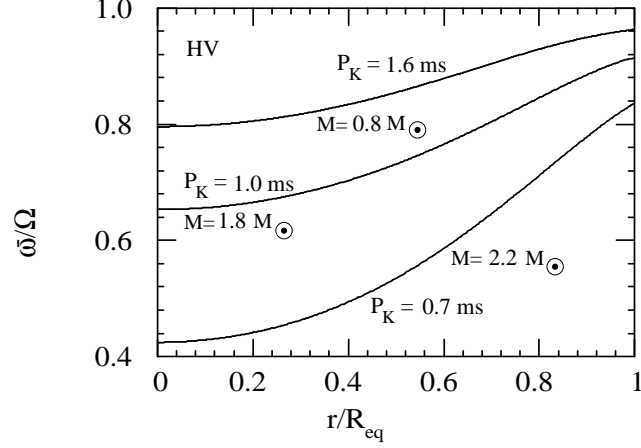


Figure 18. Dragging of the local inertial frames inside rotating neutron stars, from the center to the equator, calculated for the HV of Table 5.  $P_K$  and  $M$  denote Kepler period, defined in (50), and gravitational mass.<sup>62</sup>

Its general relativistic counterpart is given by<sup>3,115</sup>

$$\Omega_K = \omega + \frac{\omega'}{2\psi'} + e^{\nu-\psi} \sqrt{\frac{\nu'}{\psi'} + \left(\frac{\omega'}{2\psi'} e^{\psi-\nu}\right)^2}, \quad P_K \equiv \frac{2\pi}{\Omega_K}. \quad (50)$$

The primes denote derivatives with respect to the Schwarzschild radial coordinate. In order to construct stellar models that rotate at their respective Kepler frequencies, equation (50) is to be solved self-consistently together with Einstein's field equations for a given model for the equation of state.<sup>3,115</sup>

Figure 19 shows  $\Omega_K$  as a function of rotating star mass. The rectangle indicates both the approximate range of observed neutron star masses as well as the observed rotational periods which, currently, are  $P \geq 1.6$  ms. One sees that all pulsars so far observed rotate below the mass shedding frequency and so can be interpreted as rotating neutron stars. Half-millisecond periods or even smaller ones are excluded for neutron stars of mass  $1.4 M_\odot$ .<sup>3,115,116</sup> The situation appears to be very different for stars made up of self-bound strange quark matter, the so-called strange stars which will be introduced in Sect. 5. Such stars can withstand stable rotation against mass shedding down to rotational periods in the half-millisecond regime or even below.<sup>117</sup> Consequently, the possible future discovery of a single sub-millisecond pulsar spinning at say 0.5 ms could give a strong hint that strange stars actually exist, and that the deconfined self-bound phase of 3-flavor strange quark matter is in fact the true ground state of the strong interaction rather than nuclear matter.

The gravitational radiation-reaction driven instability in compact stars sets a more stringent limit on rapid stellar rotation than mass shedding, as can be seen from Figs. 20 and 21. This instability originates from counter-rotating surface vibrational modes, which at sufficiently high rotational star frequencies are dragged forward. In this case, gravitational radiation which inevitably accompanies the

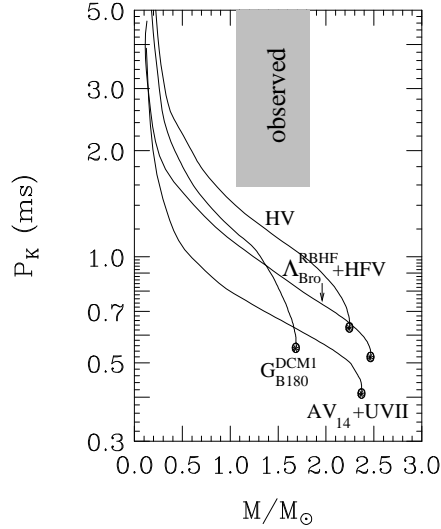


Figure 19. Onset of mass shedding from rapidly spinning neutron stars, computed for a collection of equations of state.<sup>3</sup> The Kepler period is defined in Eq. (50).

aspherical transport of matter does not damp the instability modes but rather drives them.<sup>118,119</sup> Viscosity plays the important role of damping such gravitational-wave radiation reaction-driven instabilities at a sufficiently reduced rotational frequency such that the viscous damping rate and power in gravity waves are comparable.<sup>120</sup> The instability modes are taken to have the dependence  $\exp[i\omega_m(\Omega)t + im\phi - t/\tau_m(\Omega)]$ , where  $\omega_m$  is the frequency of the surface mode which depends on the angular velocity  $\Omega$  of the star,  $\phi$  denotes the azimuthal angle, and  $\tau_m$  is the time scale for the mode which determines its growth or damping. The rotation frequency  $\Omega$  at which it changes sign is the critical frequency for the particular mode,  $m$  ( $=2,3,4,\dots$ ). It is conveniently expressed as the frequency, denoted by  $\Omega_m^\nu$ , that solves<sup>121</sup>

$$\Omega_m^\nu = \frac{\omega_m(0)}{m} \left[ \tilde{\alpha}_m(\Omega_m^\nu) + \tilde{\gamma}_m(\Omega_m^\nu) \left( \frac{\tau_{g,m}}{\tau_{\nu,m}} \right)^{\frac{1}{2m+1}} \right], \quad (51)$$

where

$$\omega_m(0) \equiv \sqrt{\frac{2m(m-1)}{2m+1} \frac{M}{R^3}} \quad (52)$$

is the frequency of the vibrational mode in a non-rotating star. The time scales for the gravitational radiation reaction to grow,  $\tau_{g,m}$ , and for viscous damping to set in,  $\tau_{\nu,m}$ , are given by<sup>3</sup>

$$\tau_{g,m} = \frac{2}{3} \frac{(m-1)[(2m+1)!!]^2}{(m+1)(m+2)} \left( \frac{2m+1}{2m(m-1)} \right)^m \left( \frac{R}{M} \right)^{m+1} R, \quad (53)$$

$$\tau_{\nu,m} = \frac{R^2}{(2m+1)(m-1)} \frac{1}{\nu}. \quad (54)$$

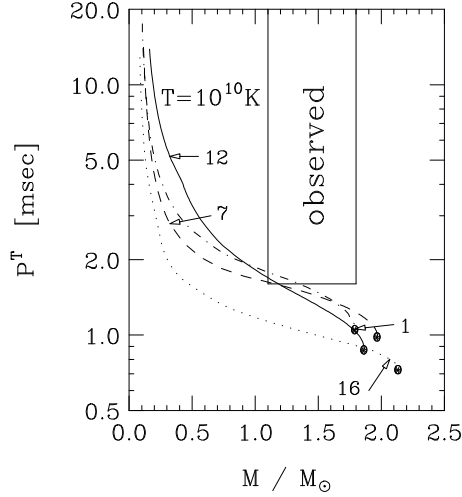


Figure 20. Gravitational radiation-reaction instability period  $P^T$  versus mass for newly born stars of temperature  $T = 10^{10}$  K.<sup>3</sup>

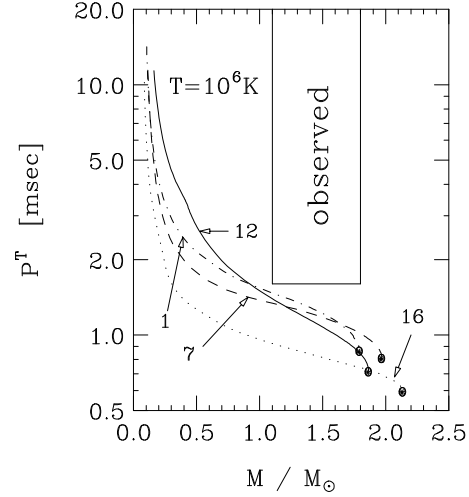


Figure 21. Gravitational radiation-reaction instability period  $P^T$  versus mass for old stars of temperature  $T = 10^6$  K.<sup>3</sup>

The shear viscosity,  $\nu$ , depends on a star's temperature according to  $\nu(T) \propto T^{-2}$ . It is small in very hot ( $T \approx 10^{10}$  K) and therefore young stars but considerably larger in cold ones ( $T \approx 10^6$  K). Information about the pulsations of the rotating star is contained in the functions  $\tilde{\alpha}_m$  and  $\tilde{\gamma}_m$ .<sup>121,122</sup> A characteristic feature of equations (51) through (54) is that  $\Omega_m^\nu$  merely depends on radius and mass ( $R$  and  $M$ ) of the spherical star model, which renders solving these equations rather straightforward.

Figure 20 shows the critical rotational periods at which the emission of gravity waves sets in in hot ( $T = 10^{10}$  K) pulsars newly born in supernova explosions. Figure 21 is the analog to Fig. 20, but for old and therefore cold pulsars of temperature  $T = 10^6$  K, like neutron stars in binary systems that are being spun up by mass accretion from a companion. One sees that the limiting rotational periods  $P^T$  ( $\equiv 2\pi/\Omega_m^\nu$ ) are the smaller the more massive (the smaller the radius) the star (cf. Fig. 16). A comparison between Figs. 20 and 21 shows that the instability periods are shifted toward smaller values the colder the star due to the larger viscosity in colder objects. Consequently, the instability modes of neutron stars in binary systems are excited at smaller rotational periods than for hot, newly born pulsars in supernovae. This conclusion hinges on the role of bulk viscosity of neutron star matter which may become very large at high temperatures. Sawyer has pointed out that it is proportional to the sixth power of the temperature as compared with a  $T^{-2}$  dependence for the shear viscosity.<sup>123</sup> This means that at temperatures  $T \gtrsim 10^9$  K the bulk viscosity may dominate over the shear viscosity and regulate the gravitational radiation-reaction driven instability in rapidly rotating neutron stars, pushing their critical rotational periods toward smaller values, possibly even as small as the Kepler period.

The dependence of  $P^T$  on the equation of state is shown too in Figs. 20 and 21

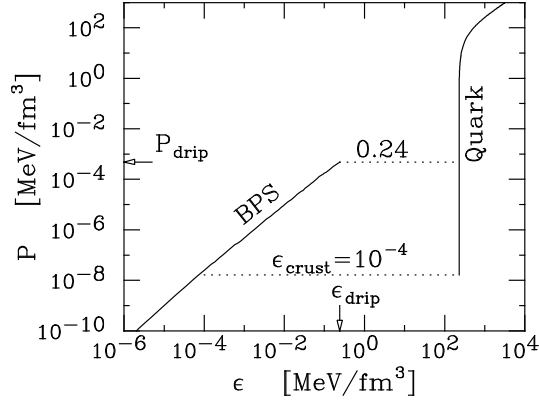


Figure 22. Equation of state of a strange star surrounded by a nuclear crust.  $P_{\text{drip}}(\epsilon_{\text{drip}})$  denotes the pressure at the maximum possible inner crust density determined by neutron drip,  $\epsilon_{\text{crust}} = 0.24 \text{ MeV/fm}^3$  ( $4.3 \times 10^{11} \text{ g/cm}^3$ ). Any inner crust value smaller than that is possible. As an example, we show the equation of state for  $\epsilon_{\text{crust}} = 10^{-4} \text{ MeV/fm}^3$  ( $10^8 \text{ g/cm}^3$ ).<sup>114</sup>

too. One sees that the lower limits on  $P^T$  are set by non-relativistic equations of state due to the relatively small radii obtained for stars constructed from them. The rectangles in Figs. 20 and 21 labeled “observed” cover both the range of observed neutron star masses,  $1.1 \lesssim M/M_{\odot} \lesssim 1.8$  as well as observed pulsar periods,  $P \geq 1.6$  ms. One sees that even the most rapidly rotating pulsars so far observed have rotational periods larger than those at which the gravitational radiation reaction-driven instability sets in. Thus all observed pulsars can be understood as rotating neutron stars. The observation of pulsars possessing masses in the observed range but rotational periods that are smaller than say  $\sim 1$  ms, depending on temperature and thus on the pulsar’s history, would be in contradiction to our collection of equations of state.

Finally, we mention the  $r$ -mode instability which has attracted a great deal of attention over the last several years. Like the  $f$ -modes discussed above, this instability too is produced by the Chandrasekhar, Friedman and Schutz (CFS) mechanism and render every star made of a perfect fluid unstable at all rates of rotation.<sup>124,125</sup> The question whether or not it provides a much more severe constraint on the stable rotation of viscous stars, however, appears to be still an open issue.

## 5 Strange Quark Matter Stars

### 5.1 The Strange Matter Hypothesis

The theoretical possibility that strange quark matter may be absolutely stable with respect to nuclear matter, that is, the energy per baryon of such matter is less than 930 MeV, has been pointed out independently by Bodmer, Terazawa, and Witten.<sup>126,127,128</sup> This so-called strange matter hypothesis constitutes one of the most startling possibilities regarding the behavior of superdense matter, which, if

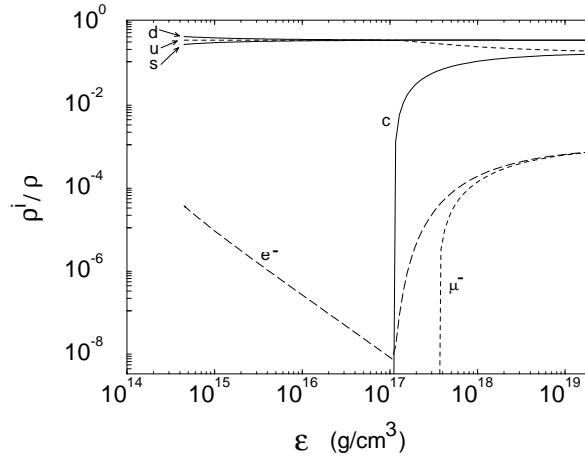


Figure 23. Relative quark and lepton densities in cold quark star matter as a function of energy density for a bag constant of  $B^{1/4} = 145$  MeV.<sup>17</sup>

true, would have implications of fundamental importance for cosmology, the early universe, its evolution to the present day, astrophysical compact objects. Even to the present day there is no sound scientific basis on which one can either confirm or reject the hypothesis so that it remains a serious possibility of fundamental significance for various phenomena.<sup>3,129</sup>

## 5.2 Quark-lepton Composition of Strange Matter

The relative quark-lepton composition of quark-star matter at zero temperature is shown in Fig. 23. All quark flavor states that become populated at the densities shown are taken into account. Strange and charm quark masses of respectively 0.15 GeV and 1.2 GeV are assumed. Since stars in their lowest energy state are electrically charge neutral to very high precision<sup>130</sup>, any net positive quark charge must be balanced by leptons. In general, as can be seen in Fig. 23, there is only little need for leptons, since charge neutrality can be achieved essentially among the quarks themselves. The concentration of electrons is largest at the lower densities of Fig. 23 due to the finite  $s$ -quark mass which leads to a deficit of net negative quark charge, and at densities beyond which the  $c$ -quark state becomes populated which increases the net positive quark charge.

The presence of electrons in strange quark matter is crucial for the possible existence of a nuclear crust on such objects, as will be discussed below. Recently it has been argued that strange quark matter is a color superconductor (see Sect. 7) which, at extremely high densities, is in the Color-Flavor-Locked (CFL) phase. This phase is rigorously electrically neutral with no electrons required.<sup>131</sup> If the CFL phase would extend all the way to the surface of a strange star, then strange stars would not be able to carry nuclear crusts because of the missing electric dipole layer. However, for sufficiently large strange quark masses, the “low” density regime of strange matter is rather expected to form a 2-flavor color superconductor (2SC)

in which electrons are present.<sup>132,133</sup>

As shown in Refs. <sup>17,134,135</sup>, the electrons, because they are bound to strange matter by the Coulomb force rather than the strong force, extend several hundred fermi beyond the surface of the strange star. Associated with this electron displacement is a electric dipole layer which can support, out of contact with the surface of the strange star, a crust of nuclear material, which it polarizes.<sup>134,135</sup> The maximal possible density at the base of the crust (inner crust density) is determined by neutron drip, which occurs at about  $4.3 \times 10^{11}$  g/cm<sup>3</sup>.

### 5.3 Equation of State of Strange Stars with Crust

The somewhat complicated situation of the structure of a strange star with crust described above can be represented by a proper choice of equation of state which consists of two parts.<sup>114</sup> At densities below neutron drip it is represented by the low-density equation of state of charge-neutral nuclear matter, for which we use the Baym-Pethick-Sutherland equation of state.<sup>136,137</sup> The star's strange matter core is described by the bag model. The graphical illustration of such an equation of state is shown in Fig. 22. Notice that there is a discontinuity in energy density between strange quark matter and hadronic matter across the electron surface (dipole gap) inside the star where the pressure of the hadronic crust at its base equals the pressure of the strange core at its surface.<sup>114</sup>

### 5.4 Strange and Charm Stars

Figure 24 shows the mass of quark matter stars as a function on central star density for different, representative bag constants. Stars with central densities smaller than a few times  $10^{15}$  g/cm<sup>3</sup> are composed of up, down and strange quarks only and are referred to as strange stars. Charm quarks are present at central densities higher than  $\sim 10^{17}$  g/cm<sup>3</sup>. Stars with densities larger than that are thus denoted charm stars. Only the sequences computed for  $B^{1/4} = 145$  MeV consist of matter that is absolutely stable at zero external pressure. The other two sequences correspond to strange matter whose energy per baryon number is about 960 MeV ( $B^{1/4} = 167$  MeV) and 1030 MeV ( $B^{1/4} = 180$  MeV). A stability analysis shows that charm stars are unstable against radial oscillations and thus cannot exist stably in the universe.<sup>138</sup> So the only type of quark stars that could possess physical significance are strange stars.

### 5.5 Complete Sequences of Strange Matter Stars

Since the nuclear crusts surrounding the cores of strange stars are bound by the gravitational force rather than confinement, the mass-radius relationship of strange matter stars with crusts is qualitatively similar to the one of purely gravitationally bound compact stars, that is, neutron stars and white dwarfs. This is illustrated in Fig. 25. The strange star sequence is computed for the maximal possible inner crust density,  $\epsilon_{\text{crust}} = \epsilon_{\text{drip}}$ . Of course there are other possible sequences of strange stars with any smaller value of inner crust density, which will be discussed below. From the maximum mass star, the central density decreases monotonically through the

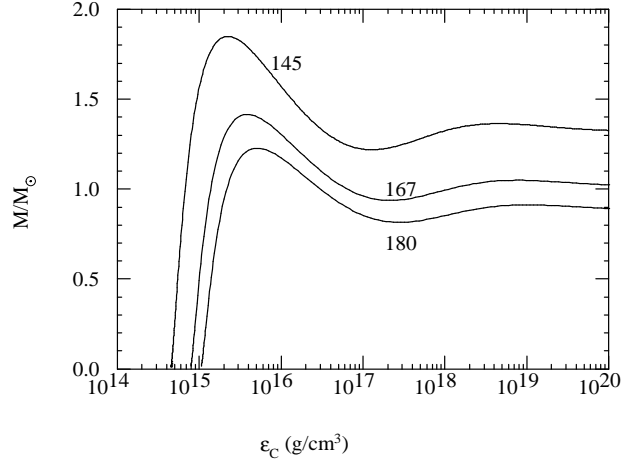


Figure 24. Gravitational mass of strange and charm stars for different  $B^{1/4}$  values.

sequence in each case. The neutron star sequence is computed for HFV of Table 5, a representative model for the equation of state of neutron star matter, which has been combined at subnuclear densities with the Baym-Pethick-Sutherland equation of state. Hence the white dwarfs shown in Fig. 25 are computed for the latter equation of state. Those gravitationally bound stars with radii  $\lesssim 200$  km and  $\gtrsim 3000$  km represent stable neutron stars and white dwarfs, respectively. The fact that strange stars with crust possess smaller radii than neutron stars leads to smaller mass shedding periods, as already indicated by the classical expression  $P_K = 2\pi\sqrt{R^3/M}$ . Of course the general relativistic expression (50), which is to be applied to neutron and strange stars, is considerably more complicated. However the qualitative dependence of  $P_K$  on mass and radius remains valid.<sup>139</sup> Due to the smaller radii of strange stars, the complete sequence of such objects (and not just those close to the mass peak, as is the case for neutron stars) can sustain extremely rapid rotation.<sup>140</sup> In particular, a strange star with a typical pulsar mass of  $\sim 1.45 M_\odot$  can rotate at Kepler periods as small as  $0.55 \lesssim P_K/\text{msec} \lesssim 0.8$ , depending on crust thickness and bag constant.<sup>114,140</sup> This range is to be compared with  $P_K \sim 1$  msec obtained for neutron stars of the same mass.<sup>141</sup>

The minimum-mass configuration of the strange star sequence, labeled “a” in Fig. 19, has a mass of about  $\sim 0.017 M_\odot$  (about 17 Jupiter masses). Depending on the chosen value of inner crust density, strange matter stars can be even by orders of magnitude lighter than this value.<sup>140</sup> If abundant enough in our Galaxy, such low-mass strange stars could be seen by the gravitational microlensing searches. Strange stars located to the right of “a” consist of small strange cores ( $\lesssim 3$  km) surrounded by a thick nuclear crust made up of white dwarf material. Such objects are thus called strange dwarfs. Their cores have shrunk to zero at the points labeled “X”. What is left is an ordinary white dwarf with a central density equal to the

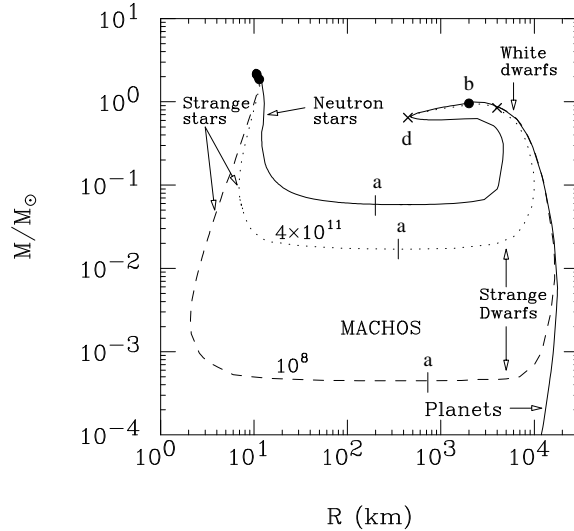


Figure 25. Mass versus radius of strange stars with nuclear crusts (dashed and dotted curves) and neutron stars and white dwarfs (solid curve). The strange stars carry nuclear crusts with chosen inner densities of  $\epsilon_{\text{crust}} = 4 \times 10^{11} \text{ g/cm}^3$  and  $10^8 \text{ g/cm}^3$ . The two crosses denote the termination points of the strange star sequences where the quark matter cores have shrunk to zero. Dots refer to maximum mass stars, minimum mass stars are located at the vertical bars labeled “a”.<sup>3</sup>

inner crust density of the former strange dwarf.<sup>140,142</sup> A detailed stability analysis of strange stars against radial oscillations shows that the strange dwarfs between “b” and “d” are unstable against the fundamental eigenmode.<sup>140</sup> Hence such objects cannot exist stably in nature. However all other stars of this sequence are stable against oscillations. So, in contrast to neutron stars and white dwarfs, the branches of strange stars and strange dwarfs are stably connected with each other.<sup>140,143</sup>

Until recently, only rather vague tests of the theoretical mass-radius relation of white dwarfs were possible. This has changed dramatically because of the availability of new data emerging from the Hipparcos project.<sup>144</sup> These data allow the first accurate measurements of white dwarf distances and, as a result, establishing the mass-radius relation of such objects empirically. Figure 26 shows a comparison of several data from the Hipparcos project with the mass-radius relationships of strange dwarfs (solid lines) and ordinary white dwarfs computed for different compositions. The outcome could suggest that there is evidence for a bimodality in the white-dwarf populations one of which may contain strange-matter cores.

### 5.6 Hadronic Crust on Strange Stars and Pulsar Glitches

Of considerable relevance for the viability of the strange matter hypothesis is the question of whether strange stars can exhibit glitches in rotation frequency. From the study performed in Refs. <sup>114,146</sup> it is known that the ratio of the crustal moment of inertia to the total moment of inertia,  $I_{\text{crust}}/I_{\text{total}}$ , varies between  $10^{-3}$  and  $\sim 10^{-5}$ . If the angular momentum of the pulsar is conserved in a stellar quake

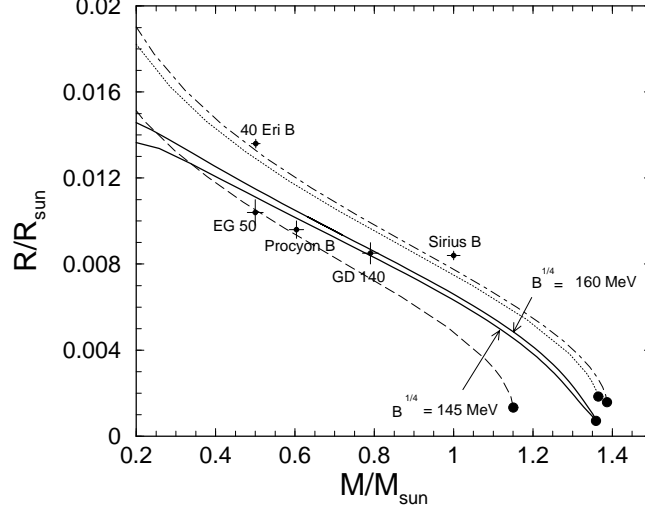


Figure 26. Comparison of theoretical mass-radius relationships of strange dwarfs ( $\epsilon_{\text{crust}} = \epsilon_{\text{drip}}$ ) and several ordinary white dwarf stars ( $^{12}\text{C}$  dwarfs: dot-dashed,  $^{24}\text{Mg}$ : dotted,  $^{56}\text{Fe}$ : dashed double-dotted) with data from the Hipparcos project.<sup>145</sup>

then the relative frequency change and moment of inertia change are equal, and one arrives for the change of the star's frequency at<sup>114</sup>

$$\frac{\Delta\Omega}{\Omega} = \frac{|\Delta I|}{I_0} > \frac{|\Delta I|}{I} \equiv f \frac{I_{\text{crust}}}{I} \sim (10^{-5} - 10^{-3})f, \text{ with } 0 < f < 1. \quad (55)$$

Here  $I_0$  denotes the moment of inertia of that part of the star whose frequency is changed in the quake. It might be that of the crust only, or some fraction, or all of the star. The factor  $f$  in Eq. (55) represents the fraction of the crustal moment of inertia that is altered in the quake, i.e.,  $f \equiv |\Delta I|/I_{\text{crust}}$ . Since the observed glitches have relative frequency changes  $\Delta\Omega/\Omega = (10^{-9} - 10^{-6})$ , a change in the crustal moment of inertia of  $f \lesssim 0.1$  would cause a giant glitch even in the least favorable case.<sup>114</sup> Moreover it turns out that the observed range of the fractional change in the spin-down rate,  $\dot{\Omega}$ , is consistent with the crust having the small moment of inertia calculated and the quake involving only a small fraction  $f$  of that, just as in Eq. (55). For this purpose we write<sup>114</sup>

$$\frac{\Delta\dot{\Omega}}{\dot{\Omega}} = \frac{\Delta\dot{\Omega}/\dot{\Omega}}{\Delta\Omega/\Omega} \frac{|\Delta I|}{I_0} = \frac{\Delta\dot{\Omega}/\dot{\Omega}}{\Delta\Omega/\Omega} f \frac{I_{\text{crust}}}{I_0} > (10^{-1} \text{ to } 10) f, \quad (56)$$

where use of Eq. (55) has been made. Equation (56) yields a small  $f$  value, i.e.,  $f < (10^{-4} \text{ to } 10^{-1})$ , in agreement with  $f \lesssim 10^{-1}$  established just above. Here measured values of the ratio  $(\Delta\Omega/\Omega)/(\Delta\dot{\Omega}/\dot{\Omega}) \sim 10^{-6} \text{ to } 10^{-4}$  for the Crab and Vela pulsars, respectively, have been used.

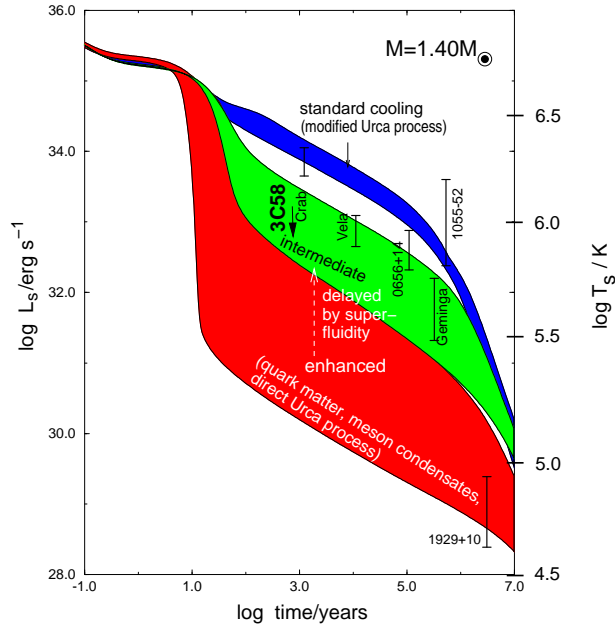


Figure 27. Cooling behavior of a  $1.4 M_{\odot}$  neutron star based on competing assumptions about the behavior of superdense matter. Three distinct cooling scenarios, referred to as “standard”, “intermediate”, and “enhanced” can be distinguished (cf. Sect. 3.7). The band-like structures reflects the uncertainties inherent in the equation of state of superdense matter.<sup>3</sup>

## 6 Thermal evolution of Neutron and Strange Stars

The predominant cooling mechanism of hot (temperatures of several  $\sim 10^{10}$  K) newly formed neutron stars immediately after formation is neutrino emission, with an initial cooling time scale of seconds. Already a few minutes after birth, the internal neutron star temperature drops to  $\sim 10^9$  K. Photon emission overtakes neutrinos only when the internal temperature has fallen to  $\sim 10^8$  K, with a corresponding surface temperature roughly two orders of magnitude smaller. Neutrino cooling dominates for at least the first  $10^3$  years, and typically for much longer in standard cooling (modified Urca) calculations. Being sensitive to the adopted nuclear equation of state, the neutron star mass, the assumed magnetic field strength, the possible existence of superfluidity, meson condensates and quark matter, theoretical cooling calculations, as summarized in Fig. 27, provide most valuable information about the interior matter and neutron star structure. The thermal evolution of a neutron star also yields information about such temperature sensitive properties as transport coefficients, transition to superfluid states, crust solidification, and internal pulsar heating mechanisms such as frictional dissipation at the crust-superfluid interfaces.<sup>147</sup> The stellar cooling tracks in Fig. 27 are computed for the broad collection of equations of state introduced in Sect. 2. Recent Chandra observations have identified pulsar J0205+6449 at the center of the young Crab-like

supernova remnant 3C58. Historical evidence suggests an association of the remnant with supernova SN 1181, which makes 3C58 younger (see Table 10) than Crab. The temperature of J0205+6449 was recently determined to be  $\log_{10} T = 6.0334$ <sup>109</sup> which, as can be seen from Fig. 27, falls well below predictions of standard cooling calculations.<sup>109</sup> Processes which speed up cooling considerably range from the presence of meson condensates<sup>13,148</sup>, to quark matter<sup>149,150</sup>, to the direct Urca process<sup>151</sup> (see Table 9 for an overview of neutron star cooling mechanisms).

## 7 Color Superconductivity of Quark Matter

There has been much recent progress in our understanding of quark matter, culminating in the discovery that if quark matter exists it will be in a color superconducting state.<sup>132,133,152,153</sup> The phase diagram of such matter is very complex.<sup>132,133</sup> At asymptotic densities the ground state of QCD with a vanishing strange quark mass is the color-flavor locked (CFL) phase. This phase is electrically neutral in bulk for a significant range of chemical potentials and strange quark masses.<sup>131</sup> If the strange quark mass is heavy enough to be ignored, then up and down quarks may pair in the two-flavor superconducting (2SC) phase. Other possible condensation patterns are the CFL- $K^0$  phase<sup>154</sup> and the color-spin locked (2SC+s) phase.<sup>155</sup> The magnitude of the gap energy lies between  $\sim 50$  and 100 MeV. Color superconductivity thus modifies the equation of state at the order  $(\Delta/\mu)^2$  level, which is only a few percent. Such small effects can be safely neglected in present determinations of models for the equation of state of neutron stars and strange quark matter stars, as is the case here. There has been much recent work on how color superconductivity in neutron stars could affect their properties. (See Refs. <sup>132,133,156,157,158,159</sup> and references therein.) These studies reveal that possible signatures include the cooling by neutrino emission, the pattern of the arrival times of supernova neutrinos, the evolution of neutron star magnetic fields, rotational (r-mode) instabilities, and glitches in rotation frequencies.

Aside from neutron star properties, an additional test of color superconductivity may be provided by upcoming cosmic ray space experiments such as AMS<sup>160</sup> and ECCO.<sup>161</sup> As shown in Ref. <sup>162</sup>, finite lumps of color-flavor locked strange quark matter (strangelets), which should be present in cosmic rays if strange matter is the ground state of the strong interaction, turn out to be significantly more stable than strangelets without color-flavor locking for wide ranges of parameters. In addition, strangelets made of CFL strange matter obey a charge-mass relation of  $Z/A \propto A^{-1/3}$ , which differs significantly from the charge-mass relation of strangelets made of “ordinary” strange quark matter. In the latter case,  $Z/A$  would be constant for small baryon numbers  $A$  and  $Z/A \propto A^{-2/3}$  for large  $A$ .<sup>129,162,163</sup> This difference may allow an experimental test of CFL locking in strange quark matter.<sup>162</sup>

## 8 Particle Thresholds and Quark Deconfinement in Rotating Neutron Stars

Figures 28 and 29 reveal that the weakening of centrifuge accompanied by the slowing-down of a rotating neutron star causes a significant increase of its central

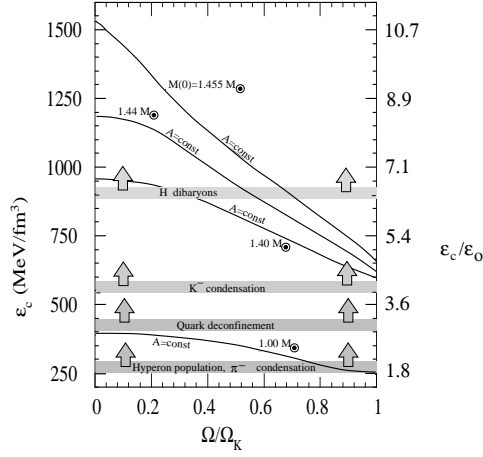


Figure 28. Central density versus rotational frequency of neutron stars of constant baryon number,  $A$ , computed for  $G_{B180}^{K300}$ . Threshold densities of various possible phases of superdense matter are indicated.  $M(0)$  is the non-rotating star mass,  $\Omega_K$  stands for the Kepler frequency.<sup>62</sup>

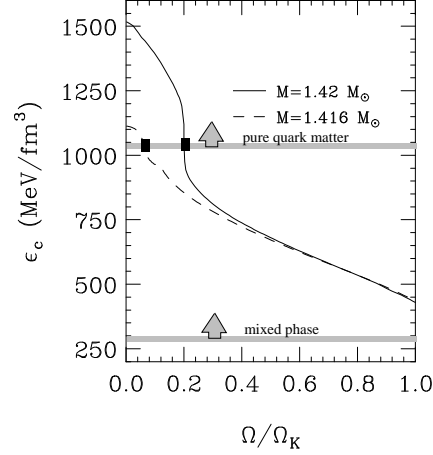


Figure 29. Central star density versus rotational frequency for two sample stars computed for equation of state  $G_{B180}^{K300}$ .

density, which is accompanied by a rearrangement of the particle population and the creation of new phases of matter. From Fig. 29, for instance, one reads off that the central density of a neutron star of mass  $M = 1.42 M_\odot$  increases from about  $450 \text{ MeV/fm}^3$  for rotation at  $\Omega_K$  to more than  $1500 \text{ MeV/fm}^3$  for  $\Omega = 0$ , which is a  $\sim 66\%$  effect. Of course, this effect is smaller for the lighter stars, since for them the changes of the gravitational pull are weaker. Such dramatic changes in the interior density of slowing-down neutron stars imply profound changes of their interior composition, because of the changing particle composition with density. Figures 30 through 33 illustrate how these changes carry over to the internal structure of conventional neutron stars. In each case the star's rotational frequency covers the maximal possible range  $0 \leq \Omega \leq \Omega_K$ . It is evident that as rotating stars spin down they become significantly less deformed, which leads to closer equality between the polar and equatorial radii. At the same time the central density rises from below to above the threshold densities of heavier baryons (i.e.,  $\Sigma$ ,  $\Lambda$ ,  $\Xi$ ). For some pulsars the mass and initial rotational frequency may be such that the central density rises from below the critical density for dissolution of baryons into their quark constituents. Examples of which are shown in Figs. 34 through 37. The evolution of the central mass densities of these stellar models can be inferred in reference with Fig. 29. For rotational frequencies below  $\sim 1250 \text{ s}^{-1}$  the quark-hybrid star models consist of an inner region of pure quark matter (q) surrounded by a few kilometer thick shell of mixed phase of hadronic and quark matter. This phase consists of structures like hadronic drops (hd), hadronic rods (hr), hadronic slabs (hs), quark slabs (qs), quark rods (qr), and quark drops (qd), in each case arranged in a lattice structure.<sup>61</sup> This shell is surrounded by a sphere of hadronic liquid (hl), itself enveloped in a

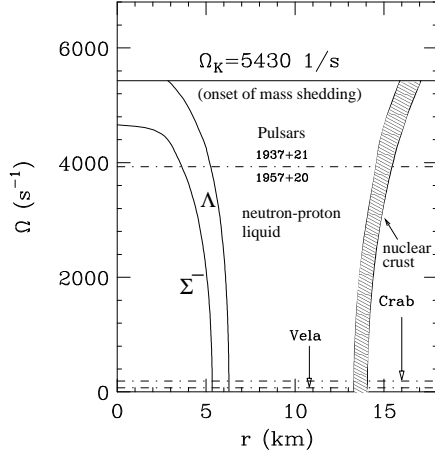


Figure 30. Frequency dependence of hyperon thresholds in equatorial neutron star direction computed for HV. The star's non-rotating mass is  $1.40 M_{\odot}$ .<sup>3</sup>

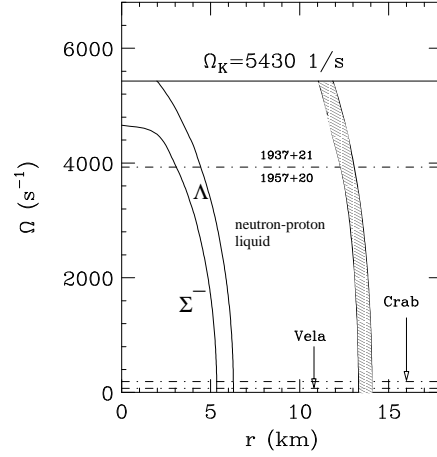


Figure 31. Same as Fig. 30, but in polar direction.<sup>3</sup>

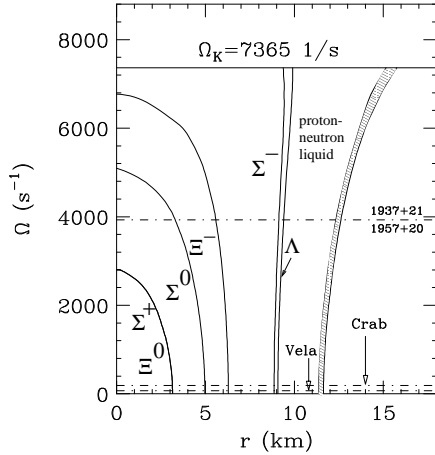


Figure 32. Frequency dependence of hyperon thresholds in equatorial neutron star direction computed for HV. The star's non-rotating mass is  $1.978 M_{\odot}$ .<sup>3</sup>

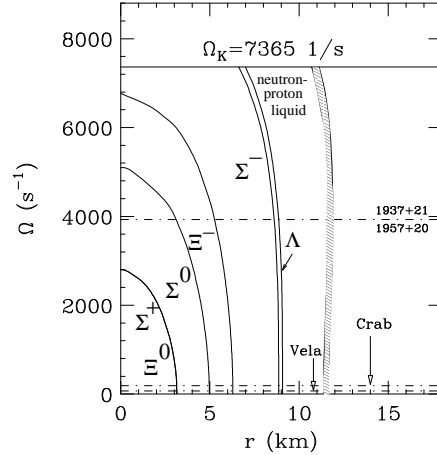


Figure 33. Same as Fig. 32, but in polar direction.<sup>3</sup>

thin nuclear crust of heavy ions. These quark-hadron structures are a consequence of the competition of the Coulomb and surface energies of the hadronic and quark matter phase.<sup>61</sup> They may have dramatic effects on pulsar observables including transport properties and the theory of glitches.

If the mass and initial rotational frequency of a pulsar is such that during its slowing-down phase the interior density rises from below to above the critical

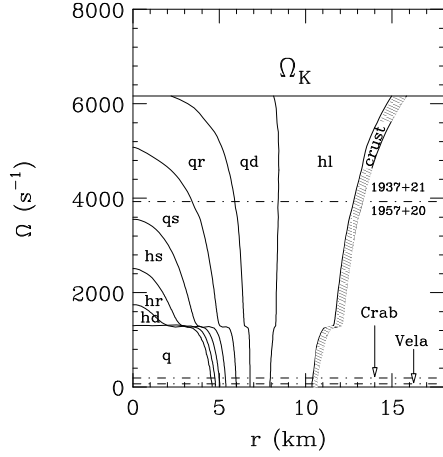


Figure 34. Frequency dependence of quark structure in equatorial neutron star direction computed for  $G_{B180}^{K300}$  and a non-rotating star mass of  $1.42 M_{\odot}$ .<sup>3</sup>

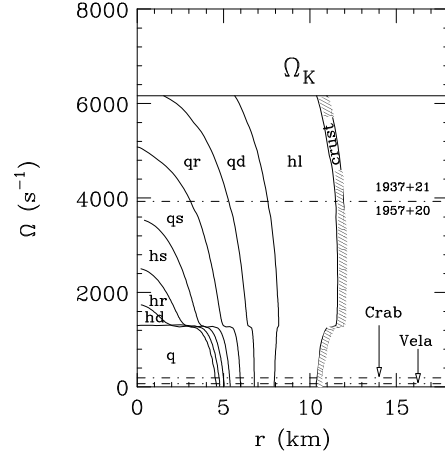


Figure 35. Same as Fig. 34, but in polar direction.<sup>3</sup>

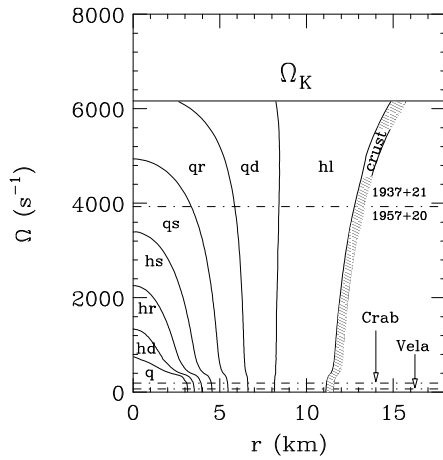


Figure 36. Frequency dependence of quark structure in equatorial direction computed for  $G_{B180}^{K300}$  and a non-rotating star mass of  $1.416 M_{\odot}$ .<sup>3</sup>

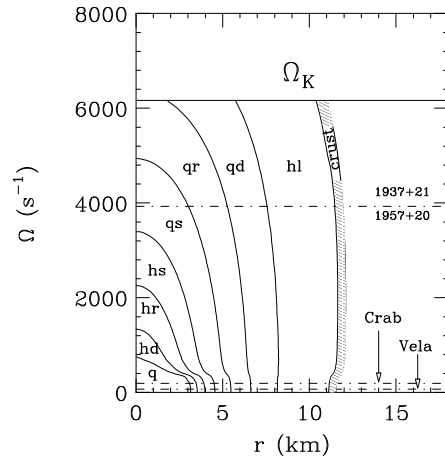


Figure 37. Same as Fig. 36, but in polar direction.<sup>3</sup>

density for the quark-hadron phase transition, first at the center where the density is highest (Figs. 28 and 29) and then in a region expanding in the radial outward direction away from the star's center, matter will be converted from the relatively incompressible nuclear matter phase to the highly compressible quark matter phase. The tremendous weight of the overlaying layers of nuclear matter tends to compress

the quark matter core, which causes the entire star to shrink on a macroscopic length scale, as shown in Figs. 34 through 37. The mass concentration in the core will be further enhanced by the increasing gravitational attraction of the quark core on the overlaying nuclear matter. The moment of inertia thus decreases anomalously with decreasing rotational frequency as the new phase slowly engulfs a growing fraction of the star<sup>164</sup>, as can be seen from Figs. 38 and 39. Figure 38 shows the moment of inertia,  $I$ , computed self-consistently from Eq. (48) for several sample stars having the same baryon number but different internal constitutions.<sup>165</sup> The curve labeled  $M = 1.420 M_{\odot}$ , computed for  $G_{B180}^{K300}$ , shows the moment of inertia of the quark-hybrid star of Figs. 34 and 35. The other curves correspond to a standard hyperon star constructed for  $G_{M78}^{K240}$  and a standard neutron star where hyperons were ignored. In accordance with what has been said just above, the shrinkage of quark-hybrid stars driven by the development of quark matter cores is the less pronounced the smaller the quark matter cores which are being built up in their centers during spin-down. Correspondingly the reduction of  $I$  weakens with decreasing star mass, as shown in Fig. 38 for several sample star masses.

The decrease of the moment of inertia caused by the quark-hadron phase transition shown in Fig. 38 is superimposed on the response of the stellar shape to a decreasing centrifugal force as the star spins down due to the loss of rotational energy. In order to conserve angular momentum not carried off by particle radiation from the star, the deceleration rate  $\dot{\Omega}$  ( $< 0$ ) must respond correspondingly by decreasing in absolute magnitude. More than that,  $\dot{\Omega}$  may even change sign, as shown in Figs. 39<sup>164</sup>, which carries the important astrophysical information that an isolated pulsar may spin up during a certain period of its stellar evolution. Such an anomalous decrease of  $I$  is analogous to the backbending phenomenon known from nuclear physics, in which case the moment of inertia of an atomic nucleus changes anomalously because of a change in phase from a nucleon spin aligned state at high angular momentum to a pair correlated superfluid phase at low angular momentum.<sup>166,167,168</sup> The stellar backbending shown in Fig. 39 shows that stars evolving from  $b \rightarrow a$  are rotationally accelerated ( $\dot{\Omega} > 0$ ), while stars evolving from  $a \rightarrow b$  are rotationally decelerated ( $\dot{\Omega} < 0$ ). The structure in the moment of inertia and, specifically, the backbending phenomenon may dramatically modify the timing structure of pulsar spin-down, rendering the observation of quark matter in neutron stars accessible to radio astronomy.

## 9 Evolution of a Pulsar's Braking Index

Pulsars are identified by their periodic signal believed to be due to a strong magnetic field fixed in the star and oriented at an angle from the rotation axis. The star's angular velocity of rotation decreases slowly but measurably over time, and usually the first and occasionally second time derivative can also be measured. Various energy loss mechanisms could be at play such as the magnetic dipole radiation, part of which is detected on each revolution, as well as other losses such as ejection of charged particles.<sup>169</sup> Without loss of generality, one can assume that pulsar slow-down is governed by a single mechanism, or several mechanisms having the same

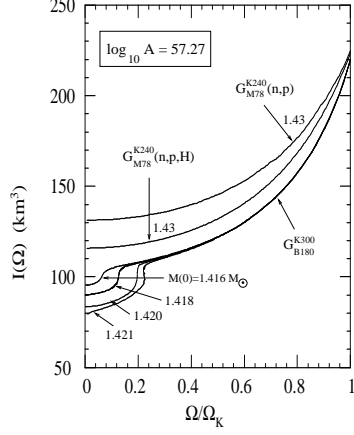


Figure 38. Moment of inertia versus frequency of neutron stars with the same baryon number,  $A$ , but different constitutions. The dips at low  $\Omega$ 's are caused by quark deconfinement.<sup>62</sup>

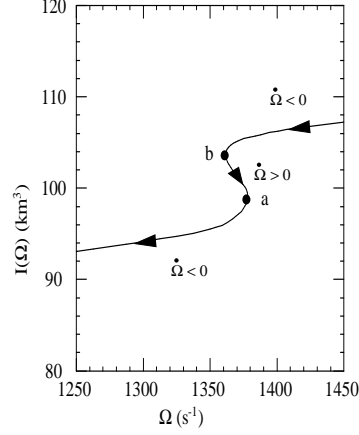


Figure 39. Enlargement of the lower-left portion of Fig. 38 for the star of mass  $M = 1.421 M_\odot$ , which is characterized by a backbending of  $I$  for frequencies between  $a$  and  $b$ .<sup>3,164</sup>

power law. The energy balance equation can then be written in the form

$$\frac{dE}{dt} = \frac{d}{dt} \left( \frac{1}{2} I(\Omega) \Omega^2 \right) = -C \Omega^{n+1}. \quad (57)$$

In the case of magnetic dipole radiation, the constant  $C$  is equal to  $C = \frac{2}{3} \mu^2 \sin^2 \alpha$  ( $\mu$  denotes the star's magnetic moment), and  $n = 3$  if  $I$  is kept constant during spin-up (down). If, as is customary, the star's angular velocity  $\Omega$  is regarded as the only time dependent quantity, one obtains the usual formula for the rate of change of the pulsar frequency, given by

$$\dot{\Omega} = -K \Omega^n, \quad (58)$$

with  $K$  a constant and  $n$  the braking index. As known from Figs. 38 and 39, the moment of inertia is not constant in time but responds to changes in rotational frequency. This response changes the value of the braking index in a frequency dependent manner, that is  $n = n(\Omega)$ . Thus during any epoch of observation, the braking index will be measured to be different from its canonical value  $n = 3$  by a certain amount. How different depends, for any given pulsar, on its rotational frequency and for different pulsars of the same frequency, on their mass and on their internal constitution. When the frequency response of the moment of inertia is taken into account, Eq. (58) is to be replaced with<sup>3,164</sup>

$$\dot{\Omega} = -2IK \frac{\Omega^n}{2I + \frac{dI}{d\Omega} \Omega} = -K \Omega^n \left( 1 - \frac{\frac{dI}{d\Omega}}{2I} \Omega + \left( \frac{\frac{dI}{d\Omega}}{2I} \Omega \right)^2 - \dots \right), \quad (59)$$

where  $K = C/I$ . This explicitly shows that the frequency dependence of  $\dot{\Omega}$  corresponding to any mechanism that absorbs (or deposits) rotational energy cannot be a simple power law as given in equation (58) (with  $K$  a constant). It must depend

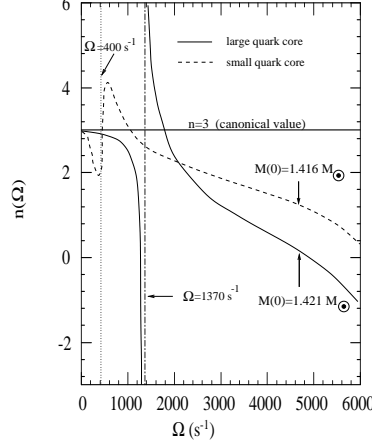


Figure 40. Braking index,  $n$ , of quark-hybrid stars of Figs. 38 and 39. The anomalies in  $n$  at  $\Omega \sim 400 \text{ s}^{-1}$  and  $\Omega \sim 1370 \text{ s}^{-1}$  are caused by quark deconfinement. The overall reduction of  $n$  below 3 is caused by the frequency dependence of the moment of inertia.<sup>62</sup>

on the mass and internal constitution of the star through the response of the moment of inertia to rotation as expressed in (59). It is interesting to note that Eq. (59) can be represented in the form of (58) but now with a frequency dependent prefactor, by evaluating

$$n(\Omega) \equiv \frac{\Omega \ddot{\Omega}}{\dot{\Omega}^2} = 3 - \frac{3 \frac{dI}{d\Omega} \Omega + \frac{d^2 I}{d\Omega^2} \Omega^2}{2I + \frac{dI}{d\Omega} \Omega}. \quad (60)$$

One sees that this effective braking index depends explicitly and implicitly on  $\Omega$  and reduces to the canonical expression  $n = 3$  only if  $I$  is independent of frequency.

As an example, we show in Fig. 40 the change of the braking index with frequency for two selected quark-hybrid stars. For illustration purposes we assume dipole radiation. Because of the structure in the moment of inertia, driven by the phase transition of baryonic matter into deconfined quark matter, the braking index deviates dramatically from  $n = 3$  at those rotational frequencies where quark deconfinement leads to the built-up of pure quark matter cores in the centers of these stars. Such anomalies in  $n(\Omega)$  are not obtained for conventional neutron stars or hyperon stars because their moments of inertia increase smoothly with  $\Omega$ , as known from Fig. 38. The observation of such an anomaly in the timing structure of pulsar spin-down could thus be interpreted as a possible signal of quark deconfinement in the center of a pulsar. Of course, because of the extremely small temporal change of a pulsar's rotational period, one cannot measure the shape of the curve which is in fact not necessary. Just a single anomalous value of  $n$  that differed significantly from the canonical value of  $n = 3$  would suffice.<sup>164,170</sup>

As a final but very important point on this subject, we estimate the typical duration over which the braking index is anomalous if deconfinement is well pro-

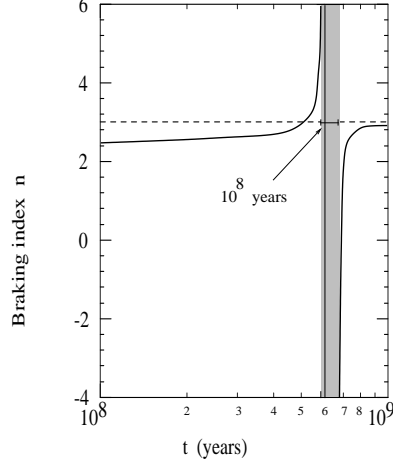


Figure 41. Braking index versus time for the quark-hybrid star of mass  $M = 1.421 M_{\odot}$  of Fig. 40. The epoch over which  $n$  is anomalous because of quark deconfinement,  $\sim 10^8$  years, is indicated by the shaded area.<sup>3</sup>

nounced. The time span can be estimated from

$$\Delta T \simeq -\frac{\Delta\Omega}{\dot{\Omega}} = \frac{\Delta P}{\dot{P}}, \quad (61)$$

where  $\Delta\Omega$  is the frequency interval of the anomaly. The range over which  $n(\Omega)$  is smaller than zero and larger than six (Fig. 40) is  $\Delta\Omega \approx -100 \text{ s}^{-1}$ , or  $\Delta P \approx -2\pi\Delta\Omega/\Omega^2 \approx 3 \times 10^{-4} \text{ s}$  at  $\Omega = 1370 \text{ s}^{-1}$ . So, for a millisecond pulsar whose period derivative is typically  $\dot{P} \simeq 10^{-19}$  one has  $\Delta T \simeq 10^8$  years, as illustrated in Fig. 41. The dipole age of such pulsars is about  $10^9$  years. So, as a rough estimate one may expect about 10% of the 25 presently known solitary millisecond pulsars to be in the transition epoch during which pure quark matter cores are gradually being built up in their centers. These pulsars could be signaling the ongoing process of quark deconfinement in their cores. Last but not least we note that the spin-up time (region  $b-a$  in Fig. 39) is about 1/5 of the time span  $\Delta T$ , or about 1/50 of the dipole age  $\tau = -\Omega/(\dot{\Omega}(n-1))$ .

It is probably needless to say that the observation of a pulsar with an anomalously large braking index, signaling the existence of quark matter in the centers of pulsars, would be a momentous discovery with most far-reaching consequences for nuclear and particle physics. It would help to clarify how quark matter behaves, and give a boost to theories about the early Universe as well as laboratory searches for the production of quark matter in heavy-ion collisions, which has become a forefront area of modern physics. On an even more fundamental level, such a discovery would prove that the essentially free quark state predicted for matter at very high energy densities actually exists, and give us a picture of an early phase of the Universe that is based on radio pulsar observation, which may be coined quark astronomy.

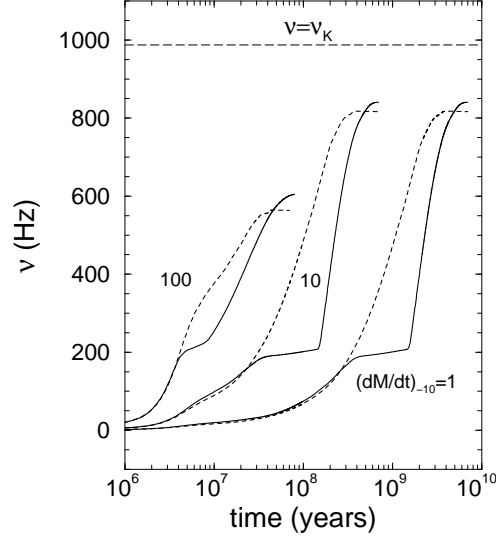


Figure 42. Evolution of spin frequencies of accreting X-ray neutron stars with (solid curves) and without (dashed curves) quark deconfinement.<sup>171</sup> The spin plateau around 200 Hz signals the ongoing process of quark re-confinement in the stellar centers

## 10 Quark Matter in Neutron Stars in Low-Mass X-ray Binaries

The signal of quark deconfinement described in Sect. 9 applies only to isolated neutron stars, where deconfinement is driven by the gradual stellar contraction as the star spins down. The situation is reversed in neutron stars in binary systems, which experience a spin-up torque because of the transfer of angular momentum carried by the matter picked up by the star's magnetic field from the surrounding accretion disk. The spin-up torque causes a change in the stars' angular momentum according to the relation<sup>171</sup>

$$\frac{dJ}{dt} = \dot{M}\tilde{l}(r_m) - N(r_c), \quad (62)$$

where  $\dot{M}$  denotes the accretion rate and

$$\tilde{l}(r_m) = \sqrt{Mr_m} \quad (63)$$

is the angular momentum added to the star per unit mass of accreted matter. The quantity  $N$  stands for the magnetic plus viscous torque term,

$$N(r_c) = \kappa \mu^2 r_c^{-3}, \quad (64)$$

with  $\mu \equiv R^3 B$  the star's magnetic moment. The quantities  $r_m$  and  $r_c$  denote the radius of the inner edge of the accretion disk and the co-rotating radius, respectively, and are given by ( $\xi \sim 1$ )

$$r_m = \xi r_A, \quad (65)$$

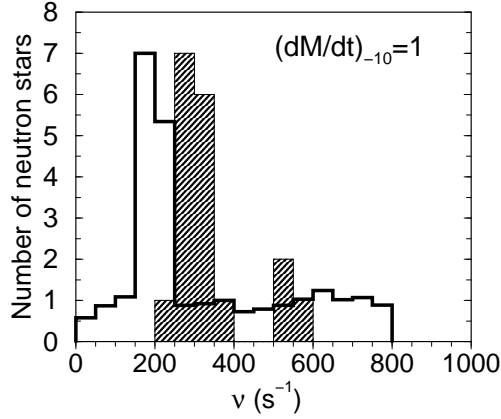


Figure 43. Calculated spin distribution of X-ray neutron stars. The spike in the calculated distribution (unshaded diagram) corresponds to the spinout of the quark matter phase. Otherwise the spike would be absent. The shaded histogram displays the observed data.<sup>171</sup>

and

$$r_c = (M\Omega^{-2})^{1/3}. \quad (66)$$

Accretion will be inhibited by a centrifugal barrier if the neutron star's magnetosphere rotates faster than the Kepler frequency at the magnetosphere. Hence  $r_m < r_c$ , otherwise accretion onto the star will cease. The Alfvén radius  $r_A$  in Eq. (65) is defined by

$$r_A = \left( \frac{\mu^4}{2M\dot{M}^2} \right)^{1/7}. \quad (67)$$

The rate of change of a star's angular frequency  $\Omega$  ( $\equiv J/I$ ) then follows from Eq. (62) as

$$I(t) \frac{d\Omega(t)}{dt} = \dot{M}\tilde{I}(t) - \Omega(t) \frac{dI(t)}{dt} - \kappa\mu(t)^2 r_c(t)^{-3}, \quad (68)$$

with the explicit time dependences as indicated. There are two terms on the right-hand-side of Eq. (68) that grow linearly respectively quadratically with  $\Omega$ . Ignoring the linear term shows that mass transfer can spin up a neutron star to an equilibrium period ( $P = 2\pi/\Omega$ ) of<sup>172</sup>

$$P_{\text{eq}} = 2.4 \text{ ms} \left( \frac{\dot{M}}{\dot{M}_{\text{Edd}}} \right)^{-3/7} \left( \frac{M}{M_{\odot}} \right)^{-5/7} R_6^{15/7} B_9^{6/7}, \quad (69)$$

where  $R_6$  and  $B_9$  are the star's radius and its magnetic field in units of  $10^6$  cm and  $10^9$  G, respectively.  $\dot{M}_{\text{Edd}}$  in Eq. (69) denotes the maximum possible accretion rate, known as the Eddington limit, at which the accretion luminosity equals the luminosity at which the radiation pressure force on ionized hydrogen plasma near the star balances the gravitational acceleration force exerted by the star on the

plasma. This condition leads to an Eddington accretion rate of  $\dot{M}_{\text{Edd}} = 1.5 \times 10^{-8} R_6 M_\odot/\text{yr}$ . For a typical accretion rate of  $\dot{M}_{-10} \equiv \dot{M}/(10^{-10} M_\odot/\text{yr})$ , the Eddington rate can be expressed as  $\dot{M}_{\text{Edd}} = 150 R_6 \dot{M}_{-10}^{-1} \dot{M}$ . The low-mass X-ray binaries (LMXBs) observed with the Rossi X-ray Timing Explorer are divided into Z sources and A(toll) sources, and appear to accrete at rates of  $\dot{M}_{-10} \sim 200$  and  $\dot{M}_{-10} \sim 2$ , respectively.

The temporal change of the moment of inertia of accreting neutron stars which undergo phase transitions is crucial for their spin evolution.<sup>171</sup> This temporal change, on the other hand, renders the computation of the moment of inertia, defined in Eq. (48), very cumbersome since each quantity on the right-hand-side of (48) varies accordingly during stellar spin-up. The solution of Eq. (68) in combination with Eq. (48) is shown in Fig. 42. The result is most striking. One sees that quark matter remains relatively dormant in the stellar core until the star has been spun up to frequencies at which the central density is about to drop below the threshold density at which quark matter exists. As known from Fig. 39, this manifests itself in a significant increase of the star's moment of inertia. The angular momentum added to a neutron star during this phase of evolution is therefore consumed by the star's expansion, inhibiting a further spin-up until the quark matter has been converted into a mixed phase of matter made up of hadrons and quarks. Such accreters, therefore, tend to spend a greater length of time in the critical frequencies than otherwise. There will be an anomalous number of accreters that appear at or near the same frequency, as shown in Fig. 43. This is what was actually found recently with the Rossi X-ray Timing Explorer (shown by the shaded area in Fig. 43). Quark deconfinement constitutes a most striking explanation for this anomaly<sup>171,173,174</sup> though alternative explanations were suggested too.<sup>175,176</sup>

## Acknowledgments

I wish to thank the organizers of Hadron 2002, Prof. Cesar A. Z. Vasconcellos and Prof. Victoria E. Herscovitz, for creating a very stimulating and enjoyable atmosphere at this meeting as well for their outstanding hospitality.

## References

1. Proceedings of the International Conference on Nuclear Physics at the Turn of the Millennium: Structure of Vacuum & Elementary Matter, ed. by H. Stöcker, A. Gallmann, and J. H. Hamilton (World Scientific, Singapore, 1997).
2. R. D. Blandford, A. Hewish, A. G. Lyne and L. Mestel (eds.), *Pulsars as Physics Laboratories*, Phil. Trans. R. Soc. Lond. A (1992) **341** 1–192.
3. F. Weber, *Pulsars as Astrophysical Laboratories for Nuclear and Particle Physics*, High Energy Physics, Cosmology and Gravitation Series (IOP Publishing, Bristol, Great Britain, 1999).
4. R. N. Manchester and J. H. Taylor, *Pulsars* (Freeman and Company, San Francisco, 1977).
5. A. G. Lyne and F. Graham-Smith, *Pulsar Astronomy* (Cambridge University Press, Cambridge, Great Britain, 1990).

6. N. K. Glendenning, *Astrophys. J.* **293** (1985) 470.
7. F. Weber and M. K. Weigel, *Nucl. Phys.* **A505** (1989) 779.
8. H. Huber, F. Weber, M. K. Weigel, and Ch. Schaab, *Int. J. Mod. Phys. E* **7**, No. 3 (1998) 301.
9. H. Umeda, K. Nomoto, S. Tsuruta, T. Muto, and T. Tatsumi, *Neutron Star Cooling and Pion Condensation*, in: *The Structure and Evolution of Neutron Stars*, ed. by D. Pines, R. Tamagaki, and S. Tsuruta (Addison-Wesley, New York, 1992) p. 406.
10. D. Kaplan and A. Nelson, *Phys. Lett.* **175B** (1986) 57.
11. G. Q. Li, C.-H. Lee, and G. E. Brown, *Nucl. Phys.* **A625** (1997) 372.
12. G. Q. Li, C.-H. Lee, and G. E. Brown, *Phys. Rev. Lett.* **79** (1997) 5214.
13. G. E. Brown, *Supernova Explosions, Black Holes and Nucleon Stars*, in: *Proceedings of the Nuclear Physics Conference – INPC '95*, ed. by S. Zuxun and X. Jincheng (World Scientific, Singapore, 1996) p. 623.
14. G. E. Brown, *Phys. Bl.* **53** (1997) 671.
15. H. Fritzsche, M. Gell-Mann, and H. Leutwyler, *Phys. Lett.* **47B** (1973) 365.
16. G. Baym, *Neutron Stars and the Physics of Matter at High Density*, in: *Nuclear Physics with Heavy Ions and Mesons*, Vol. 2, Les Houches, Session XXX, ed. by R. Balian, M. Rho and G. Ripka (North-Holland, Amsterdam, 1978) p. 745.
17. Ch. Kettner, F. Weber, M. K. Weigel, and N. K. Glendenning, *Phys. Rev. D* **51** (1995) 1440.
18. H. Heiselberg and V. Pandharipande, *Ann. Rev. Nucl. Part. Sci.* **50** (2000) 481.
19. V. R. Pandharipande, *Proc. 16th Solvay Conf. on Astrophysics and Gravitation*, Universite de Bruxelles, p. 177 (1974).
20. V. R. Pandharipande and R. B. Wiringa, *Rev. Mod. Phys.* **51** (1979) 821.
21. W. D. Myers and W. J. Swiatecki, *Nucl. Phys.* **A601** (1996) 141.
22. R. B. Wiringa, V. Fiks, and A. Fabrocini, *Phys. Rev. C* **38** (1988) 1010.
23. B. Friedman and V. R. Pandharipande, *Nucl. Phys.* **A361** (1981) 502.
24. A. Akmal, V. R. Pandharipande, and D. G. Ravenhall, *Phys. Rev. C* **58** (1998) 1804.
25. W. D. Myers and W. J. Swiatecki, *Ann. Phys. (N. Y.)* **204** (1990) 401.
26. W. D. Myers and W. J. Swiatecki, *Ann. Phys. (N. Y.)* **211** (1991) 292.
27. K. Strobel, F. Weber, M. K. Weigel, and Ch. Schaab, *Int. J. Mod. Phys. E* **6**, No. 4 (1997) 669.
28. K. Strobel, F. Weber, and M. K. Weigel, *Z. Naturforsch.* **54A** (1999) 83.
29. R. G. Seyler and C. H. Blanchard, *Phys. Rev.* **124** (1961) 227; **131** (1963) 355.
30. B. D. Serot and J. D. Walecka, *Adv. Nucl. Phys.* **16** (1986) 1.
31. R. Machleidt, K. Holinde, and Ch. Elster, *Phys. Rep.* **149** (1987) 1.
32. J. D. Bjorken and S. D. Drell, *Relativistic Quantum Fields* (Mc Graw-Hill, New York, 1965).
33. Particle Data Group, *Rev. Mod. Phys.* **56** (1984) S1.
34. T. Tatsumi and T. Muto, in: *Nuclei in the Cosmos*, ed. by H. Oberhummer and C. Rolfs (Springer-Verlag, Berlin, 1991).
35. G. E. Brown, K. Kubodera, and M. Rho, *Phys. Lett.* **192B** (1987) 273.
36. C.-H. Lee and M. Rho, *Kaon condensation in dense stellar matter*, *Proc. of*

- the International Symposium on Strangness and Quark Matter”, ed. by G. Vassiliadis, A. Panagiotou, B. S. Kumar, and J. Madsen (World Scientific, Singapore, 1995) p. 283.
37. J. A. Pons, J. A. Miralles, M. Prakash, and J. M. Lattimer, *Astrophys. J.* **553** (2001) 382.
  38. L. Wilets, *Green’s functions method for the relativistic field theory many-body problem*, in: *Mesons in Nuclei*, Vol. III, ed. by M. Rho and D. Wilkinson (North-Holland, Amsterdam, 1979) p. 791.
  39. H. Huber, F. Weber, and M. K. Weigel, *Phys. Lett.* **317B** (1993) 485.
  40. H. Huber, F. Weber, and M. K. Weigel, *Phys. Rev. C* **50** (1994) R1287.
  41. H. Huber, F. Weber, and M. K. Weigel, *Phys. Rev. C* **51** (1995) 1790.
  42. R. Brockmann and R. Machleidt, *Phys. Rev. C* **42**, (1990) 1965.
  43. C. J. Horowitz and B. D. Serot, *Nucl. Phys.* **A464** (1987) 613.
  44. N. K. Glendenning, F. Weber, and S. A. Moszkowski, *Phys. Rev. C* **45** (1992) 844.
  45. N. K. Glendenning, *Compact Stars, Nuclear Physics, Particle Physics, and General Relativity* (Springer-Verlag, New York, 1997).
  46. N. K. Glendenning, *Nucl. Phys.* **A493** (1989) 521.
  47. N. K. Glendenning, *Phys. Rev. Lett.* **57** (1986) 1120.
  48. F. Weber, N. K. Glendenning, and M. K. Weigel, *Astrophys. J.* **373** (1991) 579.
  49. R. L. Jaffe, *Phys. Lett.* **38** (1977) 195.
  50. N. K. Glendenning and J. Schaffner-Bielich, *Phys. Rev. C* **58** (1998) 1298.
  51. R. Tamagaki, *Prog. Theor. Phys.* **85** (1991) 321.
  52. T. Sakai, J. Mori, A. J. Buchmann, K. Shimizu, and K. Yazaki, *Nucl. Phys.* **A625** (1997) 192.
  53. A. Faessler, A. J. Buchmann, M. I. Krivoruchenko, and B. V. Martemyanov, *Phys. Lett.* **391B** (1997) 255.
  54. A. Faessler, A. J. Buchmann, and M. I. Krivoruchenko, *Phys. Rev. C* **56** (1997) 1576.
  55. G. Mao, P. Papazoglou, S. Hofmann, S. Schramm, H. Stöcker, and W. Greiner, *Phys. Rev. C* **59** (1999) 3381.
  56. T. Waas, M. Rho, and W. Weise, *Nucl. Phys.* **A617** (1997) 449.
  57. A. Gal, *Nucl. Phys.* **A691** (2001) 268.
  58. A. Cieply, E. Friedman, A. Gal, and J. Mares, *Nucl. Phys.* **A696** (2001) 173.
  59. N. Kaiser and W. Weise, *Phys. Lett.* **512B** (2001) 283.
  60. R. Barth et al., *Phys. Rev. Lett.* **78** (1997) 4027.
  61. N. K. Glendenning, *Phys. Rev. D* **46** (1992) 1274.
  62. F. Weber, *J. Phys. G: Nucl. Part. Phys.* **25** (1999) R195.
  63. N. K. Glendenning, *Nucl. Phys. B (Proc. Suppl.)* **24B** (1991) 110.
  64. *Physics of Neutron Star Interiors*, ed. by D. Blaschke, N. K. Glendenning, and A. Sedrakian, *Lecture Notes in Physics* **578** (Spring-Verlag, Berlin, 2001).
  65. S. E. Thorsett and D. Chakrabarty, *Astrophys. J.* **512** (1999) 288.
  66. J. H. Taylor and J. M. Weisberg, *Astrophys. J.* **345** (1989) 434.
  67. M. H. Van Kerkwijk, *Neutron Star Mass Determinations*, in: *Black Holes in Binaries and Galactic Nuclei*, ed. by L. Kaper, E. P. J. van den Heuvel, and P.

- A. Woudt (Springer-Verlag, Berlin, 2001).
68. O. Barziv, L. Kaper, M. H. van Kerkwijk, J. H. Telting, and J. van Paradijs, *Astron. & Astrophys.* **377** (2001) 925.
  69. J. A. Orosz and E. Kuulkers, *Mon. Not. R. Astron. Soc.* (in press).
  70. M. van der Klis, *Ann. Rev. Astron. Astrophys.* **38** (2000) 717.
  71. L. Burderi et al., *Astrophys. J.* **560** (2001) L71.
  72. J. Van Paradijs, *Astrophys. J.* **234** (1978) 609.
  73. S. L. Shapiro and S. A. Teukolsky, *Black Holes, White Dwarfs, and Neutron Stars* (Wiley & Sons, New York, 1983).
  74. M. Y. Fujimoto and R. E. Taam, *Astrophys. J.* **305** (1986) 246.
  75. F. M. Walter, S. J. Wolk, and R. Neuhäuser, *Nature* **379** (1996) 233.
  76. F. M. Walter and L. D. Matthews, *Nature* **389** (1997) 358.
  77. J. Drake et al., *Is RXJ1856.5-3754 a Quark Star?*, ([astro-ph/0204159](#)).
  78. J. A. Pons, F. M. Walter, J. M. Lattimer, M. Prakash, R. Neuhäuser, and P. An, *Astrophys. J.* **564** (2002) 981.
  79. F. W. Walter and J. Lattimer, *A Revised Parallax and its Implications for RXJ185635-3754*, ([astro-ph/0204199](#)).
  80. M. Ruderman, *Ann. Rev. Astron. Astrophys.* **10** (1972) 427.
  81. G. Baym and C. Pethick, *Ann. Rev. Nucl. Sci.* **25** (1975) 27.
  82. V. Trimble and M. Rees, *Astrophys. Lett.* **5** (1970) 93.
  83. G. Börner and J. M. Cohen, *Astrophys. J.* **185** (1973) 959.
  84. E. P. Liang, *Astrophys. J.* **304** (1986) 682.
  85. F. C. Michel, *Rev. Mod. Phys.* **54** (1982) 1.
  86. K. Iwasawa, K. Koyama, and J. P. Halpern, *Cyclotron Lines and the Pulse Period Change of X-ray Pulsar 1E2259+586*, in: *The Structure and Evolution of Neutron Stars*, ed. by D. Pines, R. Tamagaki, and S. Tsuruta (Addison-Wesley, New York, 1992) p. 203.
  87. J. Trümper, W. Pietsch, C. Reppin, W. Voges, R. Staubert, and E. Kendziorra, *Astrophys. J. Lett.* **219** (1978) L105.
  88. W. Voges, W. Pietsch, C. Reppin, J. Trümper, E. Kendziorra, and R. Staubert, *Astrophys. J.* **263** (1982) 803.
  89. W. Wheaton, *Nature* **282** (1979) 240.
  90. S. Chakrabarty, D. Bandyopadhyay, and S. Pal, *Phys. Rev. Lett.* **78** (1997) 2898.
  91. C. Y. Cardall, M. Prakash, and J. M. Lattimer, *Astrophys. J.* **554** (2001) 322.
  92. R. C. Duncan and C. Thompson, *Astrophys. J.* **392** (1992) L9.
  93. W. Becker, P. Predehl, J. Trümper and H. Ögelman, *IAU Circular* **5554** (1992), p. 1.
  94. J. Finley and H. Ögelman, *IAU Circular* **5787** (1993).
  95. W. Becker, *IAU Circular* **5805** (1993).
  96. W. Becker and B. Aschenbach, in: *The Lives of Neutron Stars*, ed. by M. A. Alpar, Ü. Kiziloglu, and J. Van Paradijs (Kluwer, Dordrecht, 1995) p. 47.
  97. F. Seward, F. Harnden, P. Murdin, and D. Clark, *Astrophys. J.* **267** (1983) 698.
  98. E. Trussoni, W. Brinkmann, H. Ögelman, G. Hasinger, and B. Aschenbach, *Astron. & Astrophys.* **234** (1990) 403.

99. J. P. Finley, H. Ögelman, G. Hasinger, and J. Trümper, *Astrophys. J.* **410** (1993) 323.
100. S. Safi-Harb and H. Ögelman, in: *The Lives of Neutron Stars*, ed. by M. A. Alpar, Ü. Kiziloglu, and J. Van Paradijs (Kluwer, Dordrecht, 1995) p. 53.
101. H. Ögelman, *X-Ray Observations of Cooling Neutron Stars*, in: *The Lives of Neutron Stars*, ed. by M. A. Alpar, Ü. Kiziloglu and J. Van Paradijs (Kluwer, Dordrecht, 1995) p. 101.
102. S. D. Yancopoulos, T. D. Hamilton, and D. J. Helfand, *Bull. American Astron. Soc.* **25** (1993) 912.
103. F. Seward and Z.-R. Wang, *Astrophys. J.* **332** (1988) 199.
104. W. Becker and J. Trümper, *Nature* **365** (1993) 528.
105. H. Ögelman, J. Finley and H. Zimmermann, *Nature* **361** (1993) 136.
106. J. P. Finley, H. Ögelman, and Ü. Kiziloglu, *Astrophys. J.* **394** (1992) L21.
107. J. Halpern and M. Ruderman, *Astrophys. J.* **415** (1993) 286.
108. H. Ögelman and J. Finley, *Astrophys. J.* **413** (1993) L31.
109. P. Slane, D. J. Helfand, and S. S. Murray, *New Constraints on Neutron Star Cooling from Chandra Observations of 3C58*, ([astro-ph/0204151](#)).
110. J. R. Oppenheimer and G. M. Volkoff, *Phys. Rev.* **55** (1939) 374.
111. R. C. Tolman, *Phys. Rev.* **55** (1939) 364.
112. G. E. Brown and H. A. Bethe, *Astrophys. J.* **423** (1994) 659.
113. H. A. Bethe and G. E. Brown, *Astrophys. J.* **445** (1995) L129.
114. N. K. Glendenning and F. Weber, *Astrophys. J.* **400** (1992) 647.
115. J. L. Friedman, J. R. Ipser, and L. Parker, *Astrophys. J.* **304** (1986) 115.
116. J. L. Friedman, J. R. Ipser, and L. Parker, *Phys. Rev. Lett.* **62** (1989) 3015.
117. N. K. Glendenning, *Mod. Phys. Lett.* **A5** (1990) 2197.
118. S. Chandrasekhar, *Phys. Rev. Lett.* **24** (1970) 611.
119. J. L. Friedman, *Phys. Rev. Lett.* **51** (1983) 11.
120. L. Lindblom and S. L. Detweiler, *Astrophys. J.* **211** (1977) 565.
121. L. Lindblom, *Astrophys. J.* **303** (1986) 146.
122. C. Cutler and L. Lindblom, *Astrophys. J.* **314** (1987) 234.
123. R. F. Sawyer, *Phys. Rev. D* **39** (1989) 3804.
124. N. Andersson, *Astrophys. J.* **502** (1998) 708.
125. J. L. Friedman and S. M. Morsink, *Astrophys. J.* **502** (1998) 714.
126. A. R. Bodmer, *Phys. Rev. D* **4** (1971) 1601.
127. H. Terazawa, *INS-Report-338* (INS, Univ. of Tokyo, 1979); *J. Phys. Soc. Japan*, **58** (1989) 3555; **58** (1989) 4388; **59** (1990) 1199.
128. E. Witten, *Phys. Rev. D* **30** (1984) 272.
129. *Strange Quark Matter in Physics and Astrophysics*, Proc. of the International Workshop, ed. by J. Madsen and P. Haensel, *Nucl. Phys. B (Proc. Suppl.)* **24B** (1991).
130. N. K. Glendenning, *Phys. Lett.* **114B** (1982) 392.
131. K. Rajagopal and F. Wilczek, *Phys. Rev. Lett.* **86** (2001) 3492.
132. K. Rajagopal and F. Wilczek, *The Condensed Matter Physics of QCD, At the Frontier of Particle Physics / Handbook of QCD*, ed. M. Shifman, (World Scientific) (2001), ([hep-ph/0011333](#)).
133. M. Alford, *Ann. Rev. Nucl. Part. Sci.* **51** (2001) 131.

134. C. Alcock, E. Farhi, and A. V. Olinto, *Astrophys. J.* **310** (1986) 261.
135. C. Alcock and A. V. Olinto, *Ann. Rev. Nucl. Part. Sci.* **38** (1988) 161.
136. G. Baym, C. Pethick, and P. Sutherland, *Astrophys. J.* **170** (1971) 299.
137. G. Baym, H. A. Bethe, and C. J. Pethick, *Astrophys. J.* **175** (1971) 225.
138. Ch. Kettner, F. Weber, M. K. Weigel, and N. K. Glendenning, *Stability of Strange Quark Stars with Nuclear Crust against Radial Oscillations*, Proc. of the International Symposium on Strangeness and Quark Matter, ed. by G. Vassiliadis, A. D. Panagiotou, B. S. Kumar, and J. Madsen (World Scientific, Singapore, 1995) p. 333.
139. N. K. Glendenning and F. Weber, *Phys. Rev. D* **50** (1994) 3836.
140. N. K. Glendenning, Ch. Kettner, and F. Weber, *Astrophys. J.* **450** (1995) 253.
141. F. Weber and N. K. Glendenning, *Hadronic Matter and Rotating Relativistic Neutron Stars*, Proc. of the Nankai Summer School, “Astrophysics and Neutrino Physics”, ed. by D. H. Feng, G. Z. He, and X. Q. Li (World Scientific, Singapore, 1993) p. 64–183.
142. P. F. C. Romanelli, *Strange Star Crusts*, B.S. Thesis, MIT (1986).
143. N. K. Glendenning, Ch. Kettner, and F. Weber, *Phys. Rev. Lett.* **74** (1995) 3519.
144. J. L. Provencal, H. L. Shipman, E. Hog, and P. Thejll, *Astrophys. J.* **494** (1998) 759.
145. G. J. Mathews, B. C. O’Gorman, K. Otsuki, I. Suh, and F. Weber, *Evidence for White Dwarfs with Strange-Matter Cores*, Univ. of Notre Dame preprint (2002).
146. J. L. Zdunik, P. Haensel and E. Gourgoulhon, *Astron. & Astrophys.* **372** (2001) 535.
147. Ch. Schaab, A. Sedrakian, F. Weber, and M. K. Weigel, *Astron. & Astrophys.* **346** (1999) 465.
148. D. Page, in: *The Many Faces of Neutron Stars*, ed. by R. Buccheri, J. van Paradijs, and M. A. Alpar (Kluwer Academic Publishers, Dordrecht, 1998), p. 539.
149. D. Blaschke, H. Grigorian, and D. N. Voskresensky, *Astron. & Astrophys.* **368** (2001) 561.
150. D. Page and V. V. Usov, *Thermal Evolution and Light Curves of Young Bare Strange Stars*, ([astro-ph/0204275](#)).
151. J. M. Lattimer, C. J. Pethick, M. Prakash, and P. Haensel, *Phys. Rev. Lett.* **66** (1991) 2701.
152. M. Alford, K. Rajagopal, and F. Wilczek, *Phys. Lett.* **422B** (1998) 247.
153. R. Rapp, T. Schäfer, E. V. Shuryak, and M. Velkovsky, *Phys. Rev. Lett.* **81** (1998) 53.
154. P. F. Bedaque and T. Schäfer ([hep-ph/0105150](#)).
155. T. Schäfer, *Phys. Rev. D* **62** (2000) 094007.
156. K. Rajagopal, *Acta Physica Polonica B* **31** (2000) 3021.
157. M. Alford, J. Bowers, and K. Rajagopal, *Phys. Rev. D* **63** (2001) 074016.
158. M. Alford, J. A. Bowers, and K. Rajagopal, *J. Phys. G* **27** (2001) 541.
159. D. Blaschke, D. M. Sedrakian, and K. M. Shahabasyan, *Astron. & Astrophys.* **350** (1999) L47.

160. The AMS home page is <http://ams.cern.ch>.
161. Information about ECCO can be found at <http://ultraman.berkeley.edu>.
162. J. Madsen, Phys. Rev. Lett. **87** (2001) 172003.
163. J. Madsen, Lecture Notes in Physics **516** (1999) 162.
164. N. K. Glendenning, S. Pei, and F. Weber, Phys. Rev. Lett. **79** (1997) 1603.
165. F. Weber, N. K. Glendenning, and S. Pei, *Signal for the Quark-Hadron Phase Transition in Rotating Hybrid Stars*, Proc. of the 3rd International Conference on Physics and Astrophysics of Quark-Gluon Plasma, ed. by B. C. Sinha, D. K. Srivastava, and Y. P. Viyogi (Narosa Publishing House, New Delhi, 1998) p. 237.
166. B. R. Mottelson and J. G. Valatin, Phys. Rev. Lett. **5** (1960) 511.
167. F. S. Stephens and R. S. Simon, Nucl. Phys. **A183** (1972) 257.
168. A. Johnson, H. Ryde, and S. A. Hjorth, Nucl. Phys. **A179** (1972) 753.
169. M. A. Ruderman, in: *High Energy Phenomena around Collapsed Stars*, ed. by F. Pacini (D. Reidel Publishing Company, Dordrecht, 1987).
170. N. K. Glendenning, Nucl. Phys. **A638** (1998) 239c.
171. N. K. Glendenning and F. Weber, Astrophys. J. **559** (2001) L119.
172. D. Bhattacharya and E. P. J. van den Heuvel, Phys. Rep. **203** (1991) 1.
173. N. K. Glendenning and F. Weber, *Signal of Quark Deconfinement in Millisecond Pulsars and Reconfinement in Accreting X-ray Neutron Stars*, Lecture Notes in Physics **578**, (Springer-Verlag, Berlin, 2001), p. 305.
174. G. Poghosyan, H. Grigorian, D. Blaschke, Astrophys. J. **551** (2001) L73.
175. L. Bildsten, Astrophys. J. **501** (1998) L89.
176. N. Andersson, D. I. Jones, K. D. Kokkotas, and N. Stergioulas, Astrophys. J. **534** (2000) L75.